Texas A&M University
Mechanical Engineering Department
Turbomachinery Laboratory
Tribology Group

Measurement of Static Load Performance in a Water Lubricated Hybrid Thrust Bearing

TRC-B&C-03-16

Research Progress Report to TAMU Turbomachinery Research Consortium

By

Michael Rohmer
(Former) Research Assistant

Luis San Andrés
Mast-Childs Chair Professor
Principal Investigator

Scott Wilkinson
Research Assistant

Hardik Jani
Research Assistant

May 2016
A Test Rig for Evaluation of Thrust Bearings and Face Seals
TRC Project, Maestro # 400124 00056

Executive Summary

A water lubricated thrust bearing test rig is in operating condition. Through a diaphragm coupling and quill shaft, a motor drives a rotor made of a 197 mm long 316 stainless steel shaft with two 316 stainless steel thrust collars. The shaft diameter at the location of the radial bearings is 38.1 mm, while the thrust collars have a diameter of 108 mm. Two radial hybrid bearings (4-pad flexure-pivot with diameter=38.1 mm and radial clearance=0.089 mm) support the test rotor. Presently, the test rig hosts two eight-pocket hydrostatic thrust bearings with inner diameter D_i = 40.6 mm and outer diameter D_o =76.2 mm (3 inch). One is a test bearing and the other is a slave bearing, both facing the outer side of the thrust collars on the rotor. The slave TB is affixed rigidly to a bearing support, as shown on the right of the figure. Through a non-rotating floating shaft, a load system delivers an axial load (static and/or dynamic) to the test TB. Two aerostatic bearings support the axial load shaft with minute friction. The test TB displaces to impose a load on the rotor and the slave TB reacts to this axial load.

This report extends work in Ref. [1] and discusses hydrostatic thrust bearing performance at a low (3 krpm) shaft speed. Water feeds the journal bearings at 3.45 bar(g) and the thrust bearings at various supply pressure, max. 4.14 bar(g). At each water supply pressure into the thrust bearings, the load shaft and test TB applies a load onto the rotor thrust collar, the axial clearance decreasing as the axial load increases. The reduced clearance causes an increased flow resistance across the film lands of the thrust bearing, ultimately amounting to a reduced flow rate at a large axial load. As the flow rate decreases, the pressure drop across the orifice also decreases, which results in higher recess pressures. Therefore, as the axial load increases (axial clearance decreases) with a constant water lubricant supply pressure, the supply flow rate and the flow rate through the inner diameter decrease as the recess pressure ratio increases. In addition, as the axial clearance decreases or the water supply pressure increases, the TB axial load and static stiffness increase.

XLHydroThrust® uses the TB geometry to generate predictions of bearing performance. The predictions agree with test data for flow and recess pressure. However, there are discrepancies at a high axial load (low axial clearance). As the applied axial load increases, the average percent difference between the predicted and measured magnitudes of supply flow rate, flow rate through inner diameter, axial clearance, and recess pressure ratio change from 2% to 47%, 7% to 73%, 25% to 53%, and 7% to 18%, respectively.

Construction of a closed loop water supply system enables a higher supply pressure (150 psig) and a higher flow rate (25 GPM) into the bearing. The previous arrangement sourced water from the test facility central supply and wasted it. The system utilizes a single, 7.5 HP, constant speed multi-stage vertical turbine pump to deliver water at 222 psig maximum pressure and maximum 25 GPM flow rate to the test rig. Additionally, the system includes a 2 HP, self-priming return pump for recirculation of water, an air-cooled heat exchanger to cool the water, a 500 gallon capacity reservoir tank as well as a host of valves and gauges to control and monitor flow performance. A pump shed (located outside of the test-cell) houses system components for protection from the environment. Construction of the system concluded in 2015, costing just under $9,000 (not budgeted in TRC funded proposal).

Current work includes measurements of the dynamic load performance of a water lubricated hybrid thrust bearing and identification of axial force coefficients.

Nomenclature

A	Thrust bearing area [m^2] $A = \pi\left(D_{out}^2 - D_{in}^2\right)/4$
C	Axial clearance [μm]
C_0	Axial clearance at center of thrust bearing [μm]
C_d	Empirical discharge coefficient
D	Journal bearing diameter [cm]
D_{in} , D_{out}	Thrust bearing inner and outer diameters [cm]
d_{orif}	Orifice diameter [mm]
K	Axial Stiffness [MN/m]
L	Journal bearing length [cm]
$N_{pockets}$	Number of pockets
P_a	Ambient pressure [bar(g)]
P_R	Recess pressure [bar(g)]
P_S	Water supply pressure [bar(g)]
Q_{ID}	Flow rate through inner diameter [LPM]
Q_O	Flow rate through orifice [LPM]
Q_{OD}	Flow rate through outer diameter [LPM]
Q_S	Supply flow rate [LPM]
R	Radius [cm]
R_{out}	Thrust collar outer radius [cm]
Re_{ID}	Reynolds number of flow through inner diameter
Re_{OD}	Reynolds number of flow through outer diameter
T	Temperature [°C]
W	Load [N]
δ	Tilt of thrust collar [μm/mm]
δ_X	Tilt of thrust collar about X-axis [μm/mm]
δ_Y	Tilt of thrust collar about Y-axis [μm/mm]
μ	Fluid absolute viscosity [Pa.s]

ρ	Fluid density [kg/m^3]
ω	Rotor speed [krpm]

Table of Contents

Page

List of Tables

Page

List of Figures

Page

Introduction

In rotating machinery, thrust bearings support axial loads and control shaft position. In turbomachinery, such as centrifugal compressors, axial loads depend on shaft speed, gas composition and physical properties, and operating pressure. The prediction of (impeller shroud) axial loads is largely empirical, creating the need for reliable TBs [2]. To enhance thrust bearing technology, the Texas A&M Turbomachinery Laboratory, funded by USAF (2006-2009), designed and built a thrust bearing test rig to measure the forced performance of water-lubricated thrust bearings operating at high supply pressure and high rotational speed [3]. The measurements from the test hybrid thrust bearings exhibited remarkable correlation with results from a predictive tool [4].

In 2013, the thrust bearing test rig, modified to operate with air lubricated radial bearings, experienced large amplitude vibrations leading to severe damage with loss of parts [1]. The test rig, currently fully revamped to operate with water as a lubricant, will provide reliable experimental results for various types of thrust bearings.

This report presents static load and flow rate measurements conducted on an eight-pocket TB at a rotor speed of 3 krpm ($\Omega \frac{D_{out}}{2}$ = 12 m/s). As work continues, the test rig will be used to measure the static and dynamic force performance of water lubricated hydrodynamic thrust bearings. In the future, other thrust bearing types and face seals will be assessed experimentally.

A Review of Hydrostatic Thrust Bearings

Hybrid (hydrostatic/hydrodynamic) thrust bearings (HTBs) are common in rotating machinery applications that require a high centering stiffness and accurate rotor positioning, such as precision machine tools, gyroscopes, telescopes, process fluid pumps, and other turbomachinery including cryogenic turbo pumps [5]. HTBs use an externally pressurized fluid to support (without contact) an axial load whereas hydrodynamic thrust bearings rely on shaft rotational speed to generate a hydrodynamic pressure supporting the load. Some other advantages of HTBs include a high load capacity, high damping coefficients, and no contact of bearing surfaces at low surface speeds. The load capacity, stiffness, and damping coefficients of a HTB depend on the lubricant supply pressure and the thrust collar rotational speed. Therefore, if more stiffness or load capacity are required, the supply pressure could be increased (at the expense of an increase in flow rate).

Rowe (1983) [6] describes the principle of operation of hydrostatic bearings. The fluid flow in a hydrostatic bearing overcomes two modes of flow resistance: first, the lubricant flows through a flow restrictor (orifice, capillary, constant flow valve) before coming into a recess, then it flows from the recess across a small clearance film land region. As the clearance decreases, the flow rate reduces, thus reducing the frictional head loss through the orifice. Hence, the recess pressure increases, albeit never to exceed the supply pressure (with the exception of a hydrodynamic pressure in a shallow pocket). As the recess pressure increases, the fluid pressure generates a higher reaction load between the rotor and bearing causing them to separate. Contrarily, if the axial clearance increases, the flow rate and pressure drop through the orifice also increase causing the recess pressure to decrease. As the recess pressure decreases, the fluid pressure generates a lower reaction load between the rotor and bearing causing the rotor move toward the bearing. It is by this means that a hydrostatic bearing generates a stiffness.

The geometry of the recess and the compensating flow element (orifice, capillary, constant flow valve) largely influence the performance of HTBs. Figure 1 shows four common HTB geometries. Sternlicht and Elwell (1960) [7] derive closed form design equations for the flow rate and load capacity of a single circular recess HTB and an annular multi-recess HTB, verifying their accuracy against experimental results. The authors test

both a single circular recess HTB and an annular HTB (4 recesses) using various means of flow restriction. The annular HTB has a much higher load capacity and stiffness than the single recess HTB at the same pocket pressure. HTBs with a capillary restriction have the lowest stiffness while HTBs with a constant flow restriction have the highest stiffness. Also, HTBs with a capillary restriction have a load capacity and stiffness that are independent of fluid viscosity, whereas HTBs with a constant flow rate restriction have a load capacity and stiffness that are independent of supply pressure. However, once the HTB with a constant flow restriction begins to exceed its maximum specific load (load/area), the bearing stiffness experiences a sharp cut off where it drops from its peak magnitude to zero.

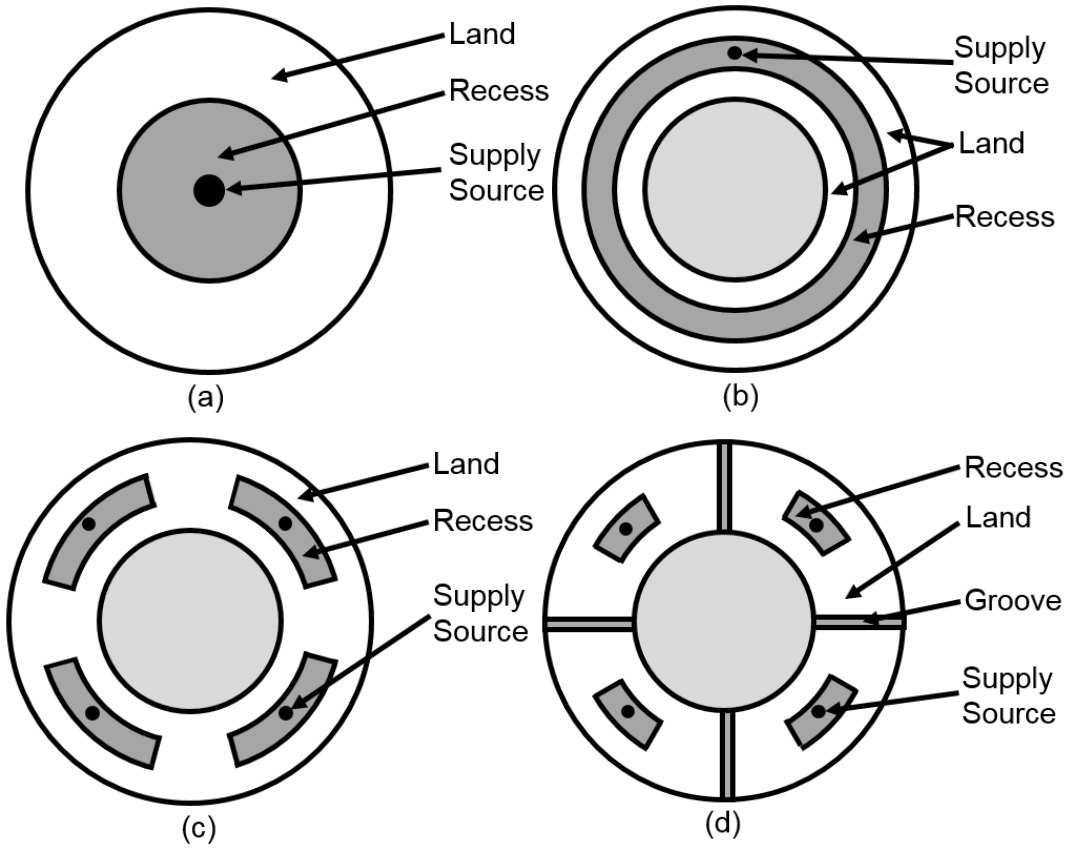

Figure 1. Common recess geometries in HTBs, including: (a) single circular recess thrust bearing, (b) annular groove thrust bearing, (c) annular multi-recess thrust bearing, and (d) multi-pad thrust bearing.

Rowe (1983) [6] calculates the load and flow rate for an incompressible fluid lubricated HTB; analytically for simple geometries such as the single circular recess HTB, and computationally for complex geometries. Rowe [6] shows annular groove HTBs demand a higher flow rate and provide a higher load capacity than a single circular recess HTB. Multi-recess HTBs have a similar load capacity and flow rate as an annular groove HTB. The multiple recess HTB produces a restoring torque when the rotor and bearing surfaces are not parallel.

Cryogenic fluid turbo pumps operate with high shaft speed and a large pressure difference. A feasible method of rotor support is to implement hybrid (hydrostatic/hydrodynamic) fluid bearings. Hybrid fluid bearings offer an economically attractive and reusable alternative to ultra-precision ceramic ball bearings, as they have no surface speed limitation or *DN* (diameter x rotor speed) limit. The advantages of hybrid bearings enable a turbo pump to be smaller, lighter, and operating with an increase in mechanical efficiency. The following references present test data to validate the performance of high-speed, high-pressure HTBs [8].

San Andrés (2000) [8] performs a bulk-flow analysis to predict the performance of a multi-recess, orifice-compensated, angled injection HTB. The application relates to cryogenic fluid turbo pumps that experience a high shaft speed (180 krpm) and a large pressure difference (550 bar). As the applied load increases, the film clearance decreases causing a decrease in flow rate and increase in recess pressure. The stiffness coefficient has an optimum value when there is a 40% pressure drop across the orifice (recess pressure is 60% of supply pressure). The damping coefficient increases as the clearance decreases or the rotational speed increases while the drag torque increases with either rotational speed or clearance. At high rotor speed and low load, centrifugal flow fluid inertia plays a significant role as it may cause fluid starvation through the bearing inner diameter and suction pressures just downstream of the edge of the recesses. The model accounting for fluid inertia at both the recesses and the film lands shows a higher damping coefficient and a lower dynamic stiffness coefficient than the model only accounting for fluid inertia

at the recesses. Fluid inertia on the bearing film land has a large effect on the bearing performance characteristics.

San Andrés (2002) [9] follows with a computational analysis to predict the performance of HTBs with angular misalignment for cryogenic fluid turbo pumps operating at a rotor speed of 180 krpm ($\mathrm{Re}_C = \rho_S \Omega R_{out} C / \mu_S = 33{,}000$) where ρ_S and μ_S are the fluid density and viscosity, Ω is the shaft rotational speed, R_{out} is the bearing outer radius, and C is the nominal axial film clearance). The static and dynamic axial stiffness as well as the static and dynamic moment-angle stiffness coefficients have a peak magnitude when the recess pressure ratio is approximately 0.6. The axial damping coefficient, the direct moment-tilt angle damping coefficient, and the cross-coupled moment stiffness coefficients slightly increase with load for low to moderate load and then increase rapidly with load for large load due to the large hydrodynamic effect at low clearance. As the misalignment angle increases, variations in recess pressure and film pressure increase, causing the overall mass flow to decrease as less flow exits through the inner diameter. In addition, both moment angle and force axial stiffness coefficients increase as the misalignment angle increases. However, the axial force and the drag torque are largely independent of the collar misalignment angle. The whirl frequency ratio (for conical rotor motions) is equal to 0.5, thus showing HTBs do not offer any added stability when compared to hydrodynamic thrust bearings.

Forsberg (2008) [3] designs and builds a test rig for water-lubricated HTBs and conducts tests with a non-rotating, HTB (8 pockets) operating with a supply pressure ranging from 3.45 bar to 17.24 bar. Figure 2 shows a cross-sectional view of the test rig, with two-flexure pivot, tilting pad radial hydrostatic bearings supporting the test rotor. The test rig uses two HTBs; a test thrust bearing and a slave thrust bearing. Both face the outer side of the thrust collars of the rotor. The slave thrust bearing is affixed rigidly to a bearing support, as shown on the right of Figure 2. A shaker delivers an axial load (static and/or dynamic) to the test thrust bearing through a non-rotating load shaft. Two aerostatic radial bearings support the axial load shaft with minimal friction for controlled displacement along the axial direction. The test thrust bearing, depicted at the center of Figure 2, moves

axially to impose a load on the rotor thrust collar. The slave thrust bearing reacts to the imposed axial load [10].

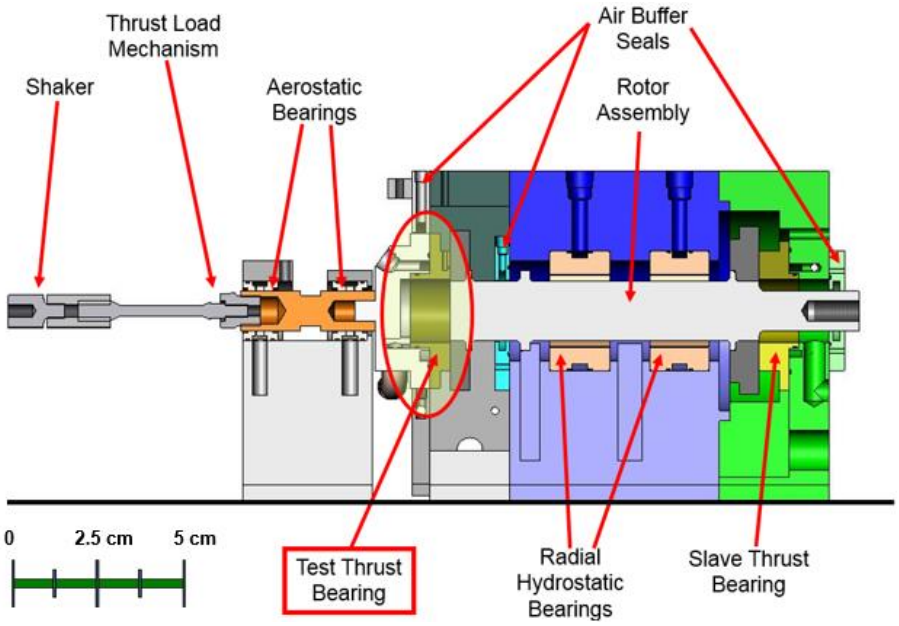

Figure 2. Cross sectional view of thrust bearing test rig. Reprinted from [10].

Forsberg [3] finds that the fluid supply pressure has a small influence on the pocket pressure ratio (ratio of pocket pressure to supply pressure). However, the pocket pressure ratio decreases significantly as the operating clearance increases (due to a smaller load) because the lubricant experiences a higher flow rate leading to a higher pressure drop across the orifice. As the supply pressure increases or the clearance decreases, the HTB develops higher pocket pressures that lead to a higher load capacity and stiffness. Most importantly, the flow rates exiting the bearing through the inner diameter and at the outer diameter are different, which could cause fluid starvation with shaft rotation. The predictions, based on a model in Ref. [9], for both the flow and load agree with measured data within 20%. However, larger discrepancies exist between the predictions and measurements of axial stiffness because of persistent misalignment of the thrust collar faces.

Ramirez (2008) [11] continues Forsberg's work to test a water-lubricated, 8 pocket HTB (8 pockets) operating at a rotor speed ranging from 7.5 krpm to 17.5 krpm and with

a supply pressure ranging from 3.45 bar to 17.24 bar. The rotor speed does not have a large effect on the bearing static stiffness or load capacity, indicating a primarily hydrostatic operation. Similar to the non-rotating condition [2], both the load and the static axial stiffness increase as either the supply pressure increases or the clearance decreases due to the higher recess pressure. Flow rate measurements through the inner diameter show the onset of fluid starvation at high rotor speed and low load due to centrifugal fluid flow acceleration. The measurements of inlet flow rate, discharge flow rate through the inner diameter, load capacity, and recess pressure ratio (ratio of recess pressure to supply pressure) differ from predictions by 1%, 5%, 7%, and 10%, respectively.

Esser (2010) [4] continues performing tests to determine the effect of orifice diameter (1.67 mm, 1.80 mm, 1.93 mm) on the performance of a water lubricated, eight pocket HTB. To this end, Esser conducts tests with the bearing operating at a rotor speed varying from 7.5 krpm to 17.5 krpm, and a supply pressure ranging from 3.45 bar to 17.24 bar. At a given load and supply pressure, the HTB experiences an increase in stiffness and enlarged operating clearance as the orifice diameter increases. While operating at a constant supply pressure, larger orifice diameter and clearance cause the supply flow rate and the exhaust flow rate through the inner diameter to increase, thus mitigating fluid starvation on the bearing inner side. When the orifice diameter increases from 1.80 mm to 1.93 mm, the thrust bearing experiences limited gains in operating clearance and axial stiffness but still requires a much higher flow rate. Overall, the predictions correlate well with measured inlet flow rate, discharge flow rate through the inner diameter, recess pressure, clearance, and axial stiffness coefficient.

San Andrés *et.* al. (2008) [10] report on the test and predictions for the performance of a HTB operating at a rotor speed of 17.5 krpm (surface speed=50 m/s) and a water lubricant supply pressure of 1.72 MPa. At a constant rotor speed, an increase in load or decrease in supply pressure causes a reduction in film clearance and flow rate. On the other hand, with a constant supply pressure, the rotor speed has little influence on the operating clearance. As the rotor speed increases and the bearing supply pressure decreases, less lubricant flows out through the inner diameter of the thrust bearing causing

lubricant starvation. Most importantly, with a rotor spinning, while the thrust bearing operates at a constant supply pressure and rotor speed, the discharge flow rate through the inner diameter rapidly decreases when the load decreases (axial clearance increases) due to centrifugal flow effects. Overall, the predictive tool estimates well the inlet flow rate, exhaust flow rate through the inner diameter, load, and film clearance when compared to measured data recorded for increasing load.

Rohmer *et.* al. (2015) [1] details a catastrophic failure (occurring in 2013) as well as many repairs and modifications to the test rig. Revamping of the test rig, completed in 2015, includes: manufacturing two new rotors, repairing the damaged threads on the housing, aligning the motor shaft centerline and the test rotor centerline, upgrading the water manifold to mitigate pressure losses, designing a load system capable of static and/or dynamic loads, installing instrumentation, and developing means of data acquisition. Measurements of the free-free mode natural frequencies and mode shapes of the rotor-coupling system show that the test rotor and quill shaft coupling must be considered as a single unit for accurate rotordynamic analysis. Without rotor speed, students measure the static load performance of a hybrid thrust bearing lubricated with water at room temperature (24 °C) and increasing supply pressure, max. 4.14 bar(g). The axial clearance increases as the water supply pressure increases for a constant load. At a constant water supply pressure, the axial clearance decreases as the axial load increases. As the axial clearance decreases, the flow rate also decreases which leads to a higher flow resistance across the film lands and a higher recess pressure.

Description of TAMU Thrust Bearing Test Rig [10]

Figure 3 shows a photograph of the thrust bearing test rig. The test rotor is a long stainless steel shaft with two stainless steel thrust collars at its ends. Two flexure pivot type radial hydrostatic bearings support the test rotor (to avoid potential hydrodynamic instability induced by shaft rotation), whose center of mass is located between the two radial bearings.

The test rig has two water lubricated hydrostatic thrust bearings; one is the test bearing (on the left of Figure 3) and the other is a slave bearing, both facing the outer side of the thrust collars on the rotor. The slave thrust bearing is affixed rigidly to a bearing support, as shown on the right of Figure 3. A load device (not shown), through a non-rotating shaft, delivers a static axial load to the test thrust bearing. Two aerostatic radial bearings support the axial load shaft with minimal friction for motions in the axial direction. The test thrust bearing moves axially to impose a load on the rotor thrust collar. This axial load is also reacted by the slave thrust bearing.

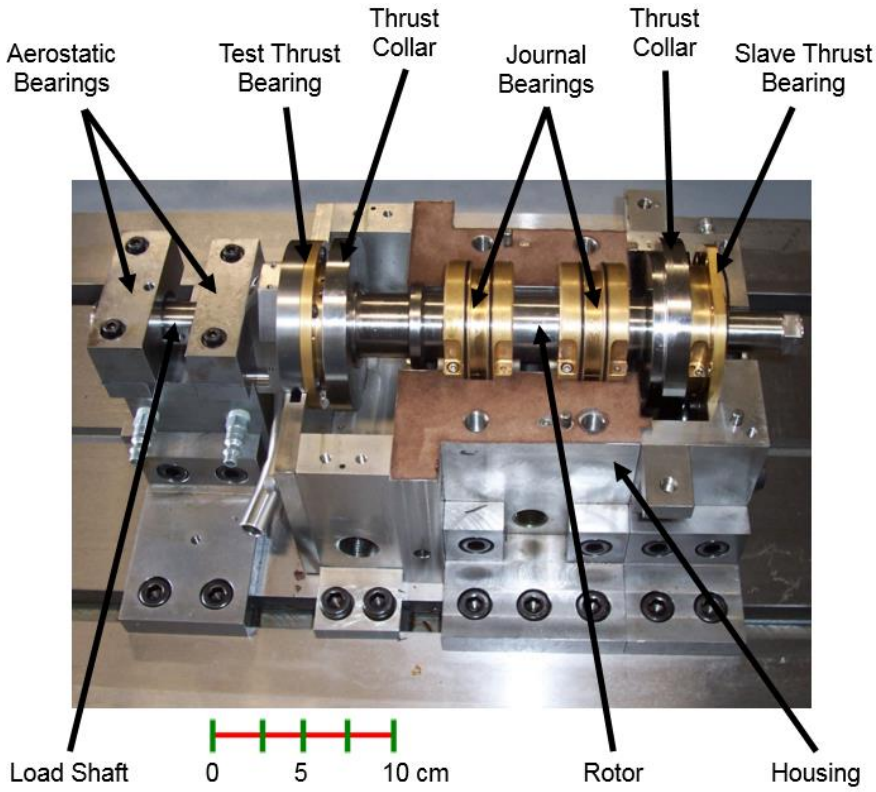

Figure 3. Photograph of hydrostatic thrust bearing test rig (2006). Reprinted from [14].

Table 1 details the radial hydrostatic/hydrodynamic bearing physical parameters and Figure 4 presents a schematic view of the bearing. The rotor comprises a 19.7 cm long 316 stainless steel shaft with two thrust disks (collars). The shaft diameter at the location of the radial bearings is 38.1 mm, and the thrust collars have an outer diameter equal to 108 mm. The electric drive motor is rated at 22 kW at a maximum operating speed of 30 krpm. The motor can deliver a constant torque, maximum 700 N-cm, over the entire speed range. A digital closed-loop speed control and a water chiller for cooling are included.

The coupling is a flexible element with quill shaft and a hub clamp. The coupling has a maximum speed rating of 30 krpm and 93.2 N-m continuous torque. In addition, the coupling has a very low axial stiffness (3.5 N/mm) with an allowance of 0.61 to 1.22 mm axial travel. These characteristics permit isolating the motor from the axial loads imposed on the thrust bearings.

The radial bearings are made of Bronze 330 and manufactured with a wired electrical discharge machining (EDM) process to render a flexure pivot – tilting pad type bearing (to avoid potential hydrodynamic instability induced by shaft rotation). The bearings are split in half for ease of installation. The radial bearing length and inner diameter equal 38.1 mm, with a machined radial clearance of 0.089 mm. A bearing has four 72° arc pads with 60% pivot offset and 20% nominal preload. Each pad contains a pocket recess for hydrostatic pressurization. The pocket dimension are 12.7 mm width, 24° arc extent, and 0.508 mm depth. The orifice for lubricant injection into the bearing is radial and at the center of a recess area. The ratio of pocket area to pad wetted area is 11% in accordance with accepted design practices for cryogenic liquid bearings. Pneumatic hammer effects are of no importance with the current bearings (radial or axial) as the fluid is water (incompressible).

Figure 5 depicts a schematic view of the test rig with its bearings as mechanical elements providing stiffness (K) and damping (C) for load support and energy dissipation, respectively.

Table 1. Dimensions and physical parameters of flexure pivot pad radial hydrostatic bearing. Material: 330 Bronze

Radial Face	Inner Diameter	1.5 inch (38.1 mm)
	Machined Radial Clearance	0.003 inch (0.076 mm)
Pads	Number of Pads	4
	Arc Length	72°
	Pivot Offset	60%
	Nominal Preload	20%
	Flexural Web moment-angle stiffness	200 N-m/rad
Pocket	Width	0.5 inch (12.7 mm)
One per pad	Arc Extent	24°
	Depth	20 mil (0.508 mm)
	Pocket/wetted area ratio	0.11
Orifice	Diameter, d_0	0.067 inch (1.7 mm)
One per pocket	Radial Location	1.08 inch (27.4 mm)

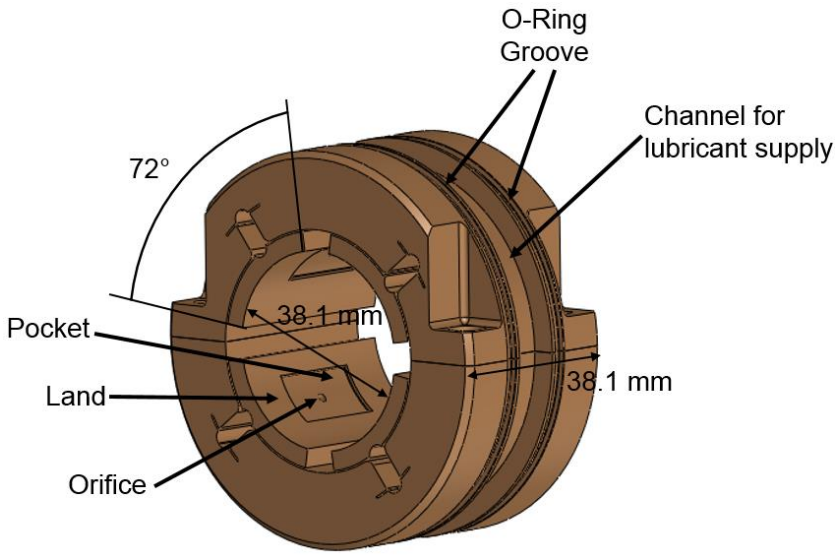

Figure 4. Depiction of water lubricated flexure pivot pad hydrostatic journal bearing [10].

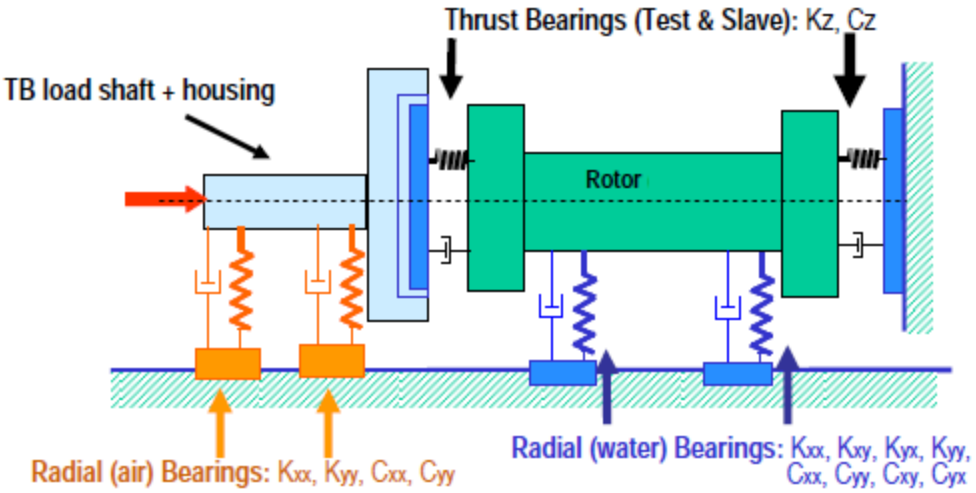

Figure 5. Schematic representation of test rig: thrust and radial bearings as mechanical elements with stiffness and damping parameters. Reprinted from [4].

Table 2 presents the material and geometric characteristics of the test and slave TBs. The slave bearing is identical to the test bearing, except that it is machined as two mating halves for ease of installation and that is has a larger orifice diameter (1.80 mm vs. 1.55 mm). The bearings have flat faces with inner and outer diameter equal to ID=40.6 mm and OD=76.2 mm, respectively. Each bearing has eight pockets, 20° arc length and 8.13 mm (0.32 inch) in radial length, uniformly distributed on the bearing circumference. The center of a pocket is located at diameter of 54.9 mm, lesser than the mid-diameter (58.4 mm), to reduce the spurious effects of centrifugal flow at high rotational speeds. The orifice injection is axial, i.e., perpendicular to the TB face.

Table 2. Dimensions and physical parameters of hydrostatic thrust bearings. Material: 660 Bearing Bronze

Thrust Face	Inner Diameter, D_{in}	1.6 inch (40.6 mm)
	Outer Diameter, D_{out}	3.0 inch (76.2 mm)
	Area, $A = \pi({D_{out}}^2 - {D_{in}}^2)/4$	5.06 in^2 (32.6 cm^2)
	Flange Outer Diameter	3.88 inch (98.5 mm)
Pocket 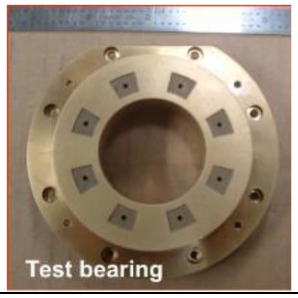	Number of Pockets	8
	Arc Length	20°
	Radial Length	0.32 inch (8.13 mm)
	Depth	20 mil (0.508 mm)
	Mean Diameter	2.16 inch (54.9 mm)
	Pocket/wetted area ratio	0.19
	Inlet loss coefficient from pocket to land	0.20
Orifice One per pocket	Diameter, d_{orif} (Slave TB)	0.071 inch (1.8 mm)
	Diameter, d_{orif} (Test TB)	0.061 inch (1.55 mm)
	Radial Location	1.08 inch (27.4 mm)
	Entrance Loss Coefficient, C_d	0.58-0.62 (from tests)

Thrust Bearing Performance for Tests with a Low Rotor Speed

Prior to initiating shaft rotation, pressurized water (T=31 °C) supplies the journal bearings at 3.45 bar(g) and lifts the rotor. Note that the water temperature is higher than in previous measurements (T=24 °C previously) without shaft rotation because the external temperature (pipes are located outdoors) is higher. Water at 2.76 bar(g) supplies the slave and test thrust bearings. The static loader applies a load onto the test thrust bearing, which transfers the load to the rotor thrust collar. The slave thrust bearing, rigidly affixed to the housing, reacts to the applied load. The static loader applies a maximum net load (356 N, W/A=10.92 bar) onto the thrust bearings without contact between the rotor and the thrust bearings.

Considering that the rotor spins freely (by hand), the motor accelerates the rotor/coupling assembly to 3 krpm (50 Hz), which corresponds to a surface speed $(\Omega\frac{D_{out}}{2})$ of 12 m/s on the edge of lubricated thrust collar area $(\frac{D_{out}}{2})$. With a constant lubricant supply pressure into the thrust bearings, the static loader decreases the applied

axial load. Note that the test procedure involves only decreasing the applied load, so the clearance of the thrust bearing only increases while the rotor is spinning at 3 krpm, thus avoiding potential contact between the rotor thrust collar and thrust bearing surfaces with rotor rotation. The above procedure is repeated for water (31 °C) feeding the thrust bearings at a supply pressure (P_S) of 2.76, 3.45, and 4.14 bar(g) with an axial load ranging from 90 to 450 N. Thus, the specific axial load (W/A) ranges from 0.3 to 1.4 bar. Note A=32.6 cm^2 = $\frac{1}{4}\pi(D_{out}^2 - D_{in}^2)$.

For tests with a rotor speed of 3 krpm, figures 6-9 show the axial clearance at the center (C_0) of the test and slave thrust bearings, the axial load applied onto the thrust bearings, and the thrust collar tilt (δ) about each axis of the test and slave thrust bearings versus time and frequency, respectively. The test rig operates with 3.45 bar(g) water (31 °C) supplying the thrust bearing and an average specific load (W/A) of 0.80 bar applied on the thrust bearing. The axial load remains relatively constant with respect to time and frequency. The axial clearance at the center of each thrust bearing is largely constant with a small amplitude at 50 Hz (3 krpm). However, the thrust collar tilt about each axis relative to each thrust bearing varies periodically at a frequency of 50 Hz (3 krpm). Thus, as the rotor spins, the orientation of the thrust collar changes relative to the thrust bearing housing. The amplitude of the tilt is the same for both the test and slave thrust bearings, showing that the rotor moves as a rigid piece.

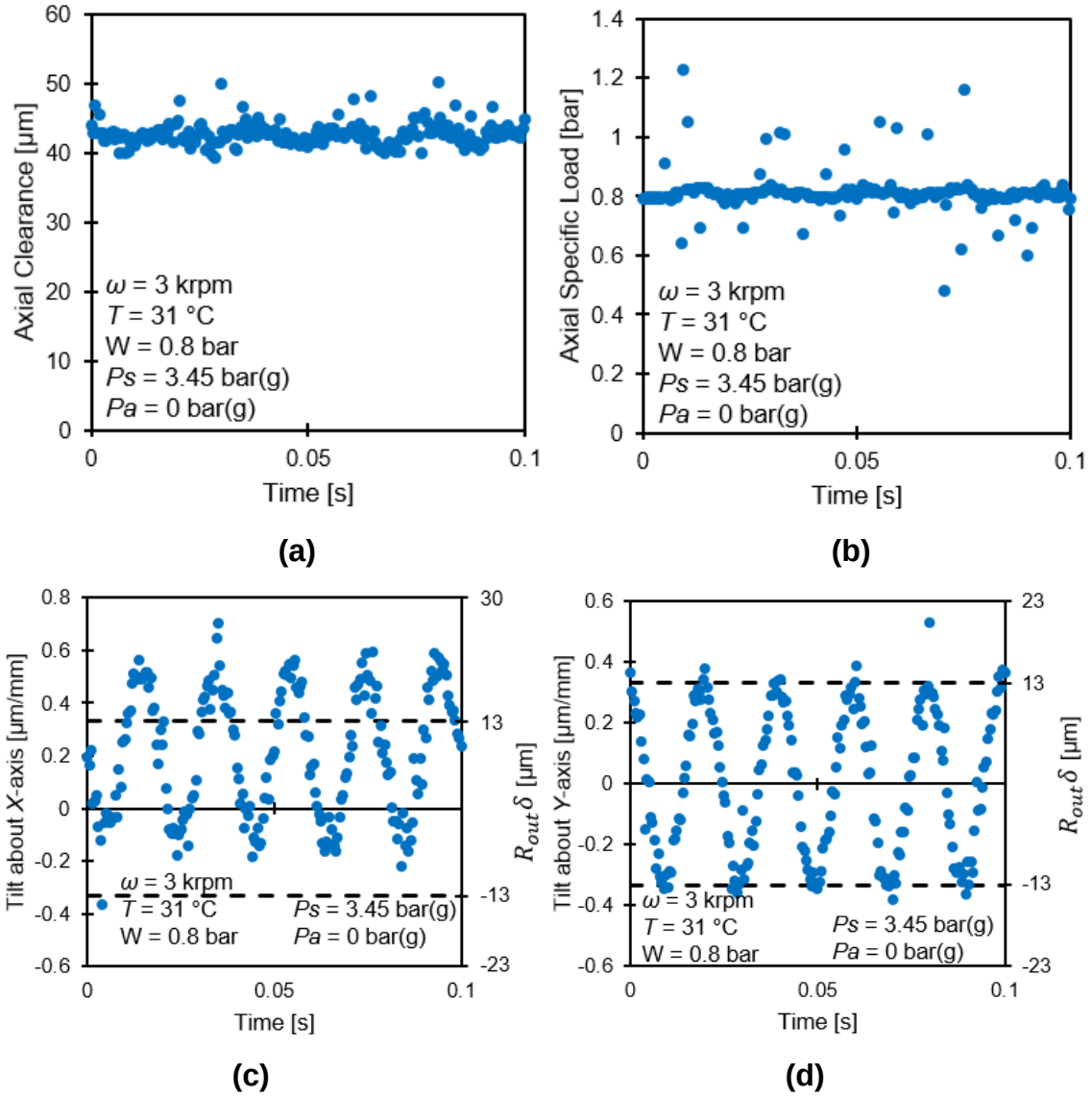

Figure 6. Estimated (a) axial clearance between test thrust bearing and thrust collar, tilt of thrust collar about (c) *X*-axis and (d) *Y*-axis relative to test thrust bearing, and (b) measured specific axial load vs. time for operation with water (31 °C) at a supply pressure (P_S) of 3.45 bar(g) into the thrust bearing. Shaft rotates at 3 krpm. Specific axial load (*W/A*) is 0.80 bar. Water at 3.45 bar(g) feeds the journal bearings. Ambient pressure (P_a) is 0 bar(g).

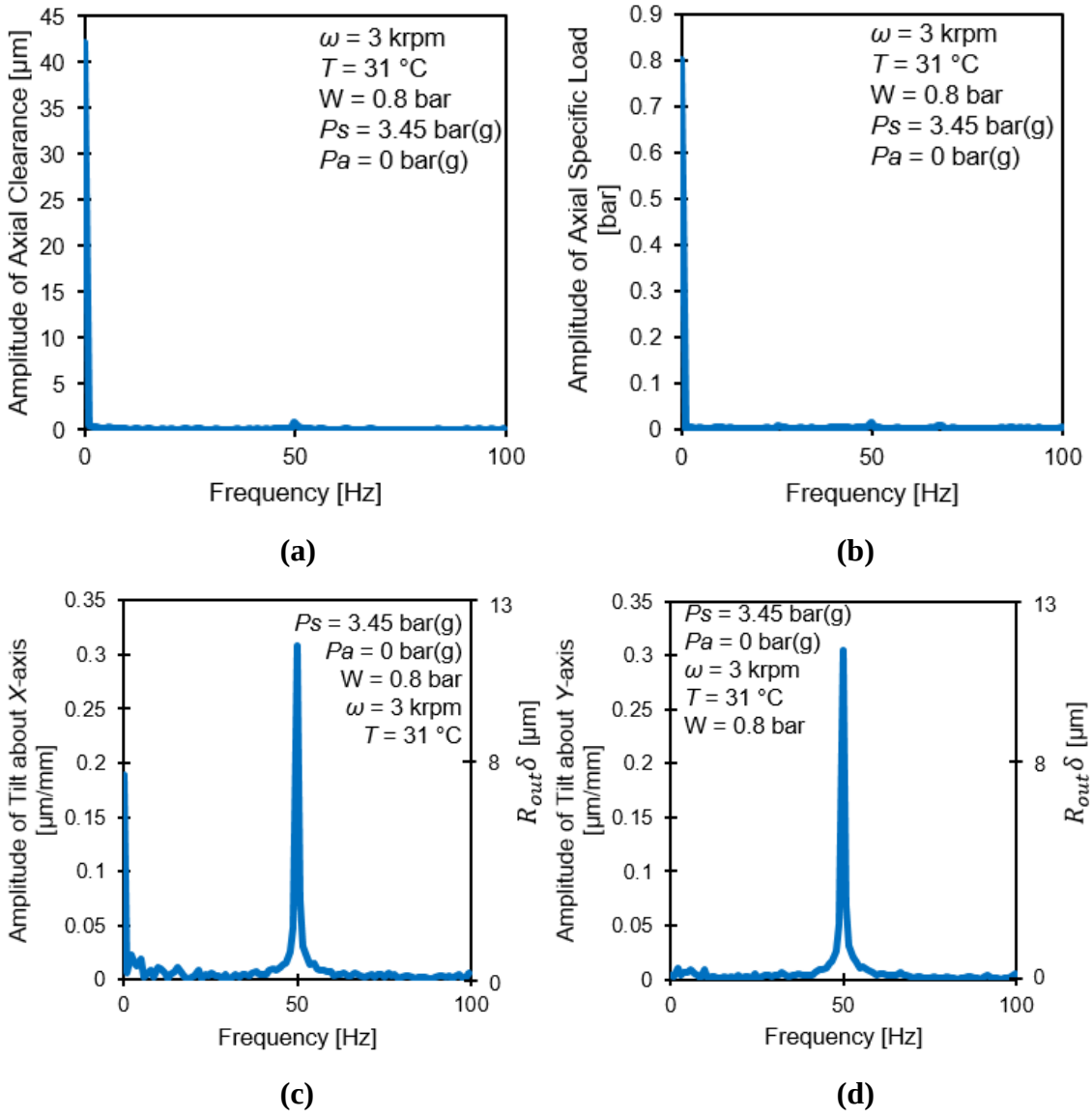

Figure 7. Amplitude of estimated (a) axial clearance between test thrust bearing and thrust collar, tilt of thrust collar about (c) *X*-axis and (d) *Y*-axis relative to test thrust bearing, and (b) measured specific axial load vs. frequency for operation with water (31 °C) at a supply pressure (P_S) of 3.45 bar(g) into the thrust bearing. Shaft rotates at 3 krpm. Specific axial load (W/A) is 0.80 bar. Water at 3.45 bar(g) feeds the journal bearings. Ambient pressure (P_a) is 0 bar(g).

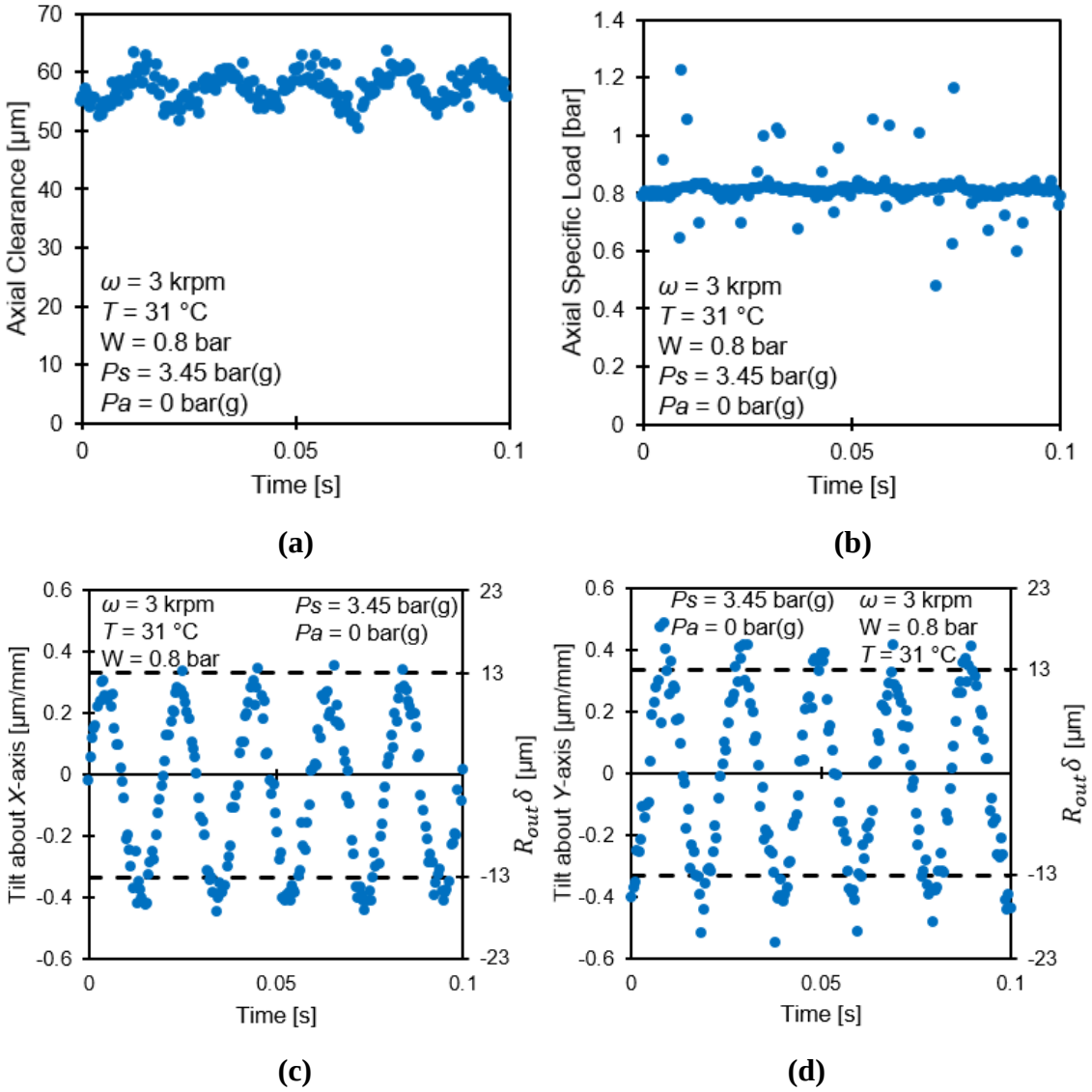

Figure 8. Estimated (a) axial clearance between slave thrust bearing and thrust collar, tilt of thrust collar about (c) *X*-axis and (d) *Y*-axis relative to slave thrust bearing, and (b) measured specific axial load vs. time for operation with water (31 °C) at a supply pressure (P_S) of 3.45 bar(g) into the thrust bearing. Shaft rotates at 3 krpm. Specific axial load (*W/A*) is 0.80 bar. Water at 3.45 bar(g) feeds the journal bearings. Ambient pressure (P_a) is 0 bar(g).

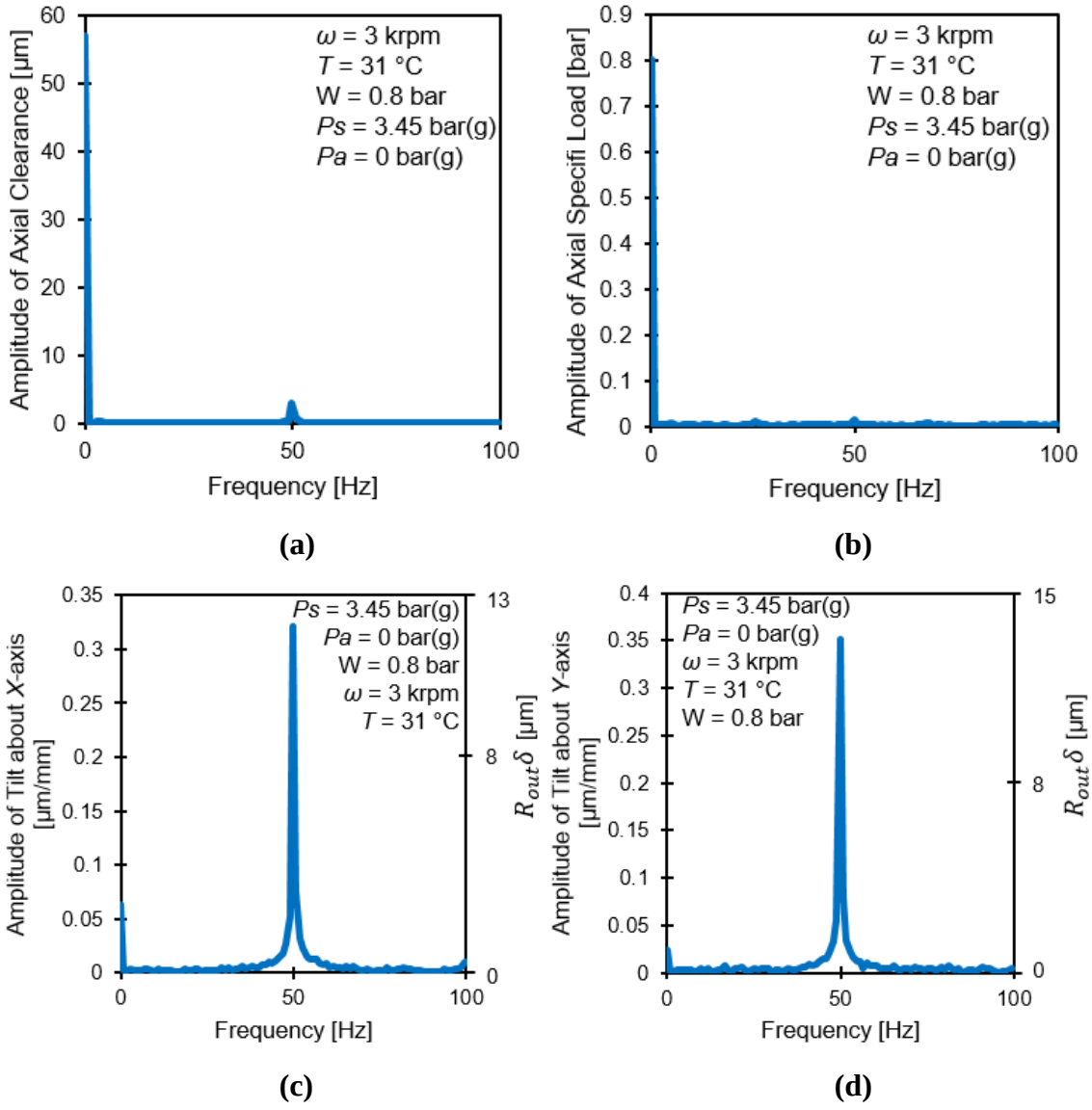

Figure 9. Amplitude of estimated (a) axial clearance between slave thrust bearing and thrust collar, tilt of thrust collar about (c) *X*-axis and (d) *Y*-axis relative to slave thrust bearing, and (b) measured specific axial load vs. frequency for operation with water (31 °C) at a supply pressure (P_S) of 3.45 bar(g) into the thrust bearing. Shaft rotates at 3 krpm. Specific axial load (*W/A*) is 0.80 bar. Water at 3.45 bar(g) feeds the journal bearings. Ambient pressure (P_a) is 0 bar(g).

For operation with water at 2.76, 3.45, and 4.14 bar(g) supplying the thrust bearings and with a rotor spinning at 3 krpm (50 Hz), Figures 10 and 11 show the misalignment (δ [µm/mm]) of the test and slave thrust bearings relative to their corresponding thrust collar, respectively. The thrust bearings are aligned with the rotor thrust collars so that the mean

of the maximum deviation in axial clearance across each thrust bearing surface is less than ±13 μm for the vast majority of imposed loads.

However, Figures 10 and 11 also show that there is a large difference between the maximum and minimum misalignment angles of each thrust bearing. Although the average orientation of each thrust collar indicates acceptable alignment with its corresponding thrust bearing, there are instances when the thrust collar may have a significantly different alignment than its average orientation. The large difference between the maximum and minimum misalignment angles arises from a motion synchronous with rotor speed that causes the orientation of the thrust collar relative to the thrust bearing to change as the rotor spins.

Stiffer radial and thrust bearings (higher supply pressure and lower clearance) would mitigate variations in the thrust collar orientation. Note that as the axial clearance decreases, the difference between the maximum and minimum axial clearance on the face of the thrust bearing also decreases; thus, showing that a smaller axial clearance provides more tilt stiffness to variations in the thrust collar angular orientation.

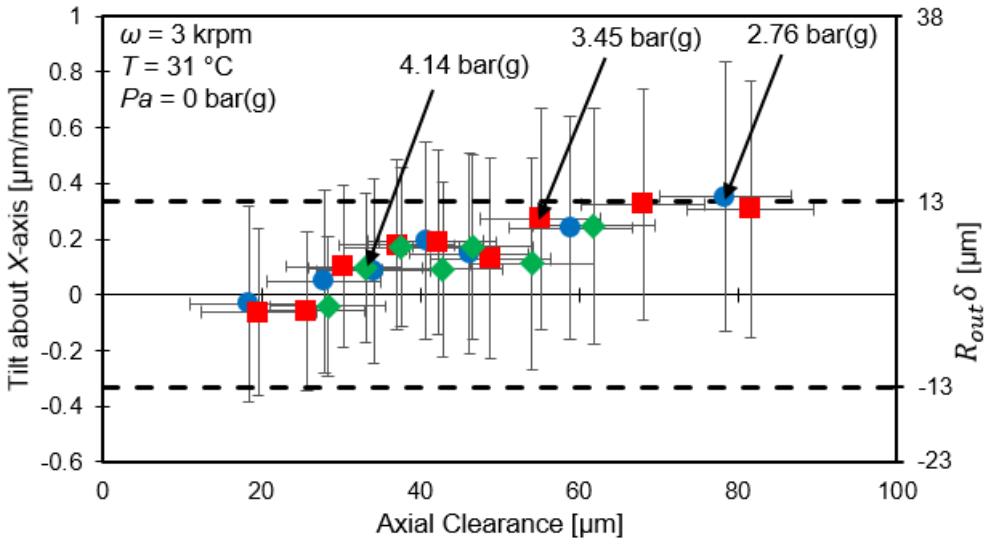

(a)

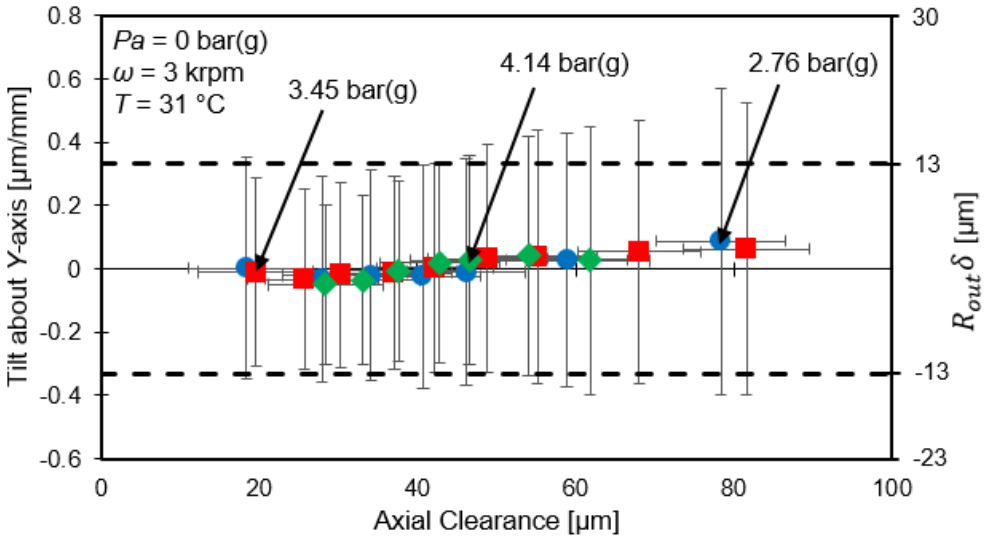

(b)

Figure 10. Estimated misalignment (µm/mm) between test thrust bearing and thrust collar about (a) *X*-axis and (b) *Y*-axis vs. estimated axial clearance at the center of the test thrust bearing for operation with water (31 °C) at a supply pressure (P_S) of 2.76, 3.45, and 4.14 bar(g) into the thrust bearing. Shaft rotates at 3 krpm. Specific axial load (*W*/*A*) ranges from 0.26 bar to 1.41 bar. Water at 3.45 bar(g) feeds the journal bearings. Ambient pressure (P_a) is 0 bar(g). Horizontal error bars represent the uncertainty in the clearance at the center of the test thrust bearing at a 95% confidence level. Vertical error bars indicate the maximum and minimum thrust collar tilt about each axis relative to the face of the thrust bearing. Dashed lines indicate the misalignment slope that corresponds with ±13 µm deviation in axial clearance over the surface of the test thrust bearing.

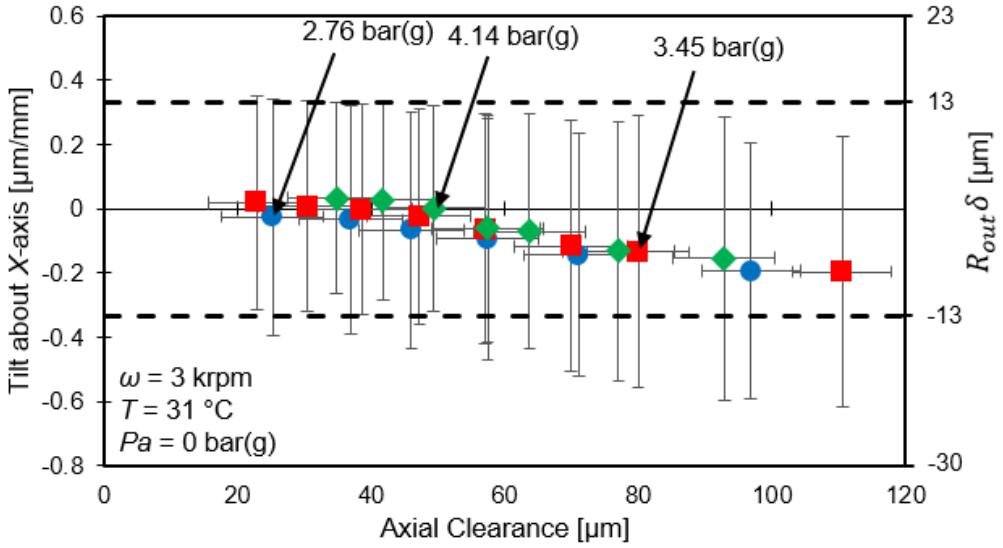

(a)

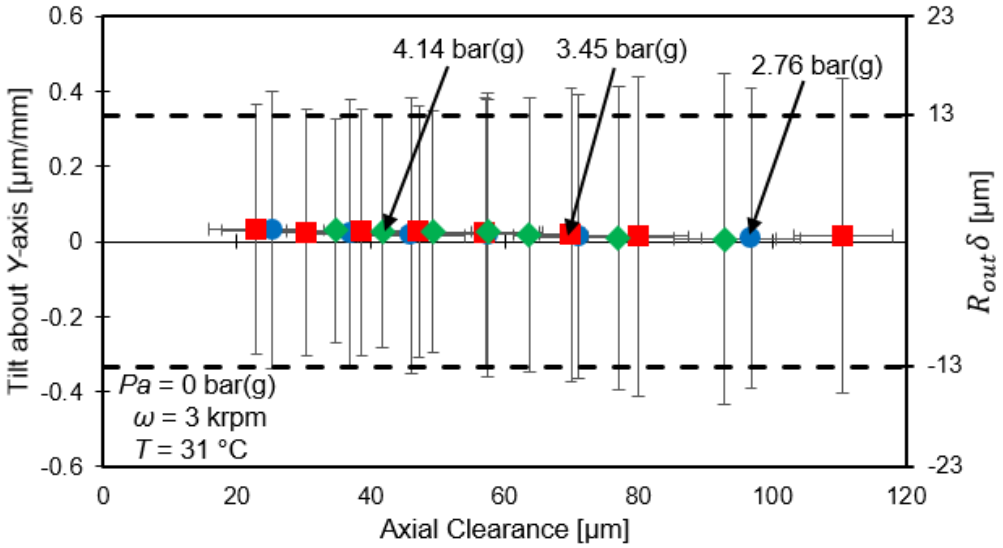

(b)

Figure 11. Estimated misalignment (µm/mm) between slave thrust bearing and thrust collar about (a) *X*-axis and (b) *Y*-axis vs. estimated axial clearance at the center of the slave thrust bearing for operation with water (31 °C) at a supply pressure (P_S) of 2.76, 3.45, and 4.14 bar(g) into the thrust bearing. Shaft rotates at 3 krpm. Specific axial load (*W*/*A*) ranges from 0.26 bar to 1.41 bar. Water at 3.45 bar(g) feeds the journal bearings. Ambient pressure (P_a) is 0 bar(g). Horizontal error bars represent the uncertainty in the clearance at the center of the slave thrust bearing at a 95% confidence level. Vertical error bars indicate the maximum and minimum thrust collar tilt about each axis relative to the face of the thrust bearing. Dashed lines indicate the misalignment slope that corresponds with ±13 µm deviation in axial clearance over the surface of the slave thrust bearing.

Figure 12 shows the axial clearance (C_0) at the center of the (a) test TB and (b) slave TB, respectively, versus specific load (W/A) for operation with rotor speed at 3 krpm ($\Omega \frac{D_{out}}{2}$ = 12 m/s) and a supply pressure of 2.76, 3.45, and 4.14 bar(g) into the thrust bearings. At a constant load, the axial clearance of each thrust bearing increases as the water pressure supplied to the thrust bearings increases. However, the specific load (W/A) is only a fraction of the water pressure supplied to the thrust bearings. At each water supply pressure, the axial clearance of each thrust bearing decreases as the specific axial load increases. The slave thrust bearing operates with a much larger axial clearance than the test thrust bearing for operation at the same load and water supply pressure. The slave thrust bearing also operates at a larger clearance than the test thrust bearing when the rotor is not spinning. This is because the slave thrust bearing has orifices with a diameter 16% larger than the orifices in the test thrust bearing (see Table 4). Measurements show a high uncertainty in the load measured by the strain gauge load cell while the motor is running. The strain gauge is more susceptible to electrical noise than other instruments because of its low voltage output (< 30 mV).

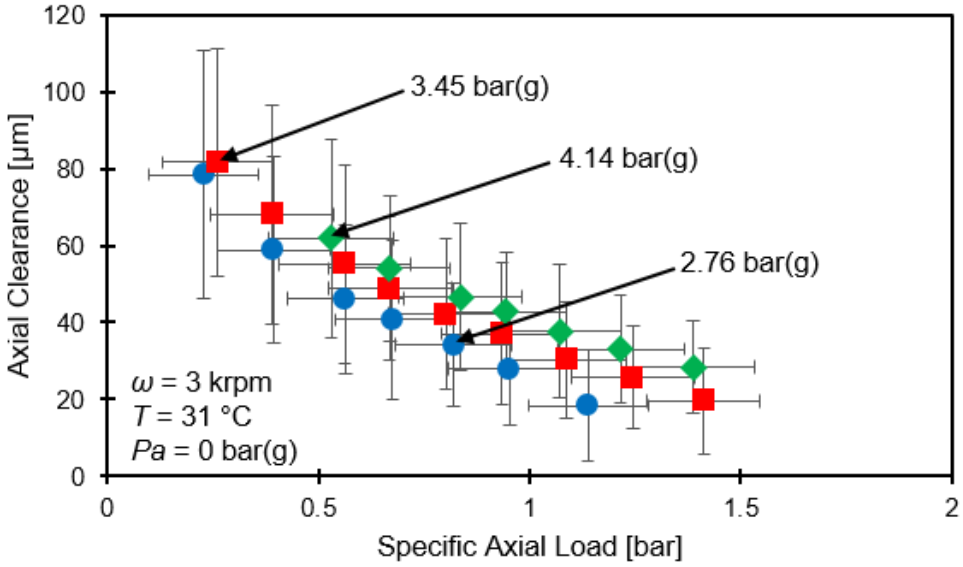

(a) Test Thrust Bearing

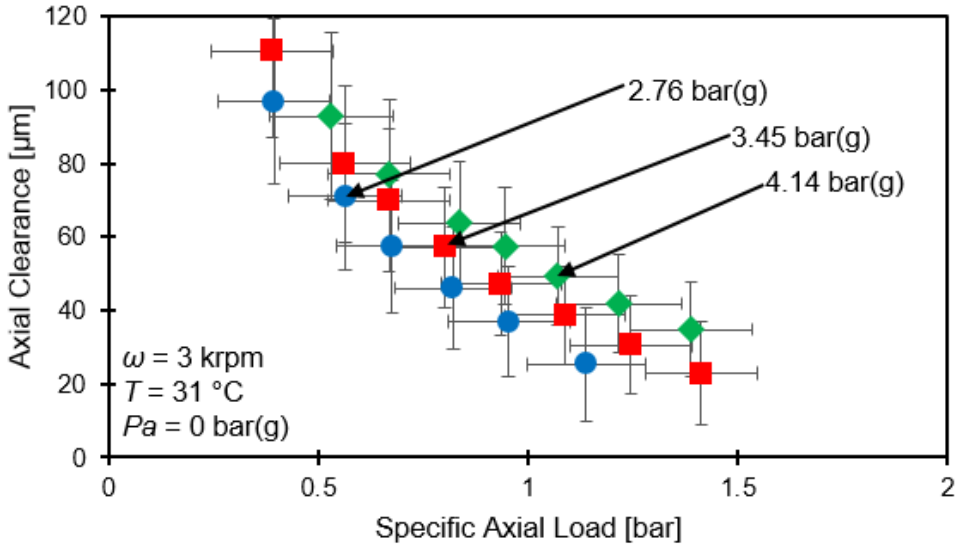

(b) Slave Thrust Bearing

Figure 12. Estimated axial clearance at the center of (a) test thrust bearing and (b) slave thrust bearing vs. specific load (*W/A*) for operation with water (31 °C) at a supply pressure (P_S) of 2.76, 3.45, and 4.14 bar(g) into the thrust bearing. Shaft rotates at 3 krpm. Water at 3.45 bar(g) feeds the journal bearings. Ambient pressure (P_a) is 0 bar(g). Horizontal error bars represent the uncertainty in the axial load at a 95% confidence level. Vertical error bars indicate the maximum and minimum clearances on the face of the thrust bearing.

Figure 13 shows the axial clearance (C_0) at the center of the test and slave thrust bearings versus specific axial load (*W/A*), respectively, for operation at a rotor speed of 0

and 3 krpm as water at 2.76 bar(g), 3.45 bar(g), and 4.14 bar(g) supplies the thrust bearings, respectively. At each water supply pressure, the rotor speed does not have an effect on the axial clearance at a high axial clearance (low load). However, at a low axial clearance (high axial load), the thrust bearings operating with a rotor speed of 3 krpm operate at a slightly larger clearance. Overall, the data show each thrust bearing operates mainly as a hydrostatic bearing. It should be noted that the water inlet temperature is several degrees cooler (7 °C) during tests without rotor speed when compared to the measurements of bearing performance at a rotor speed of 3 krpm, i.e. T = 24°C vs. T = 31°C.

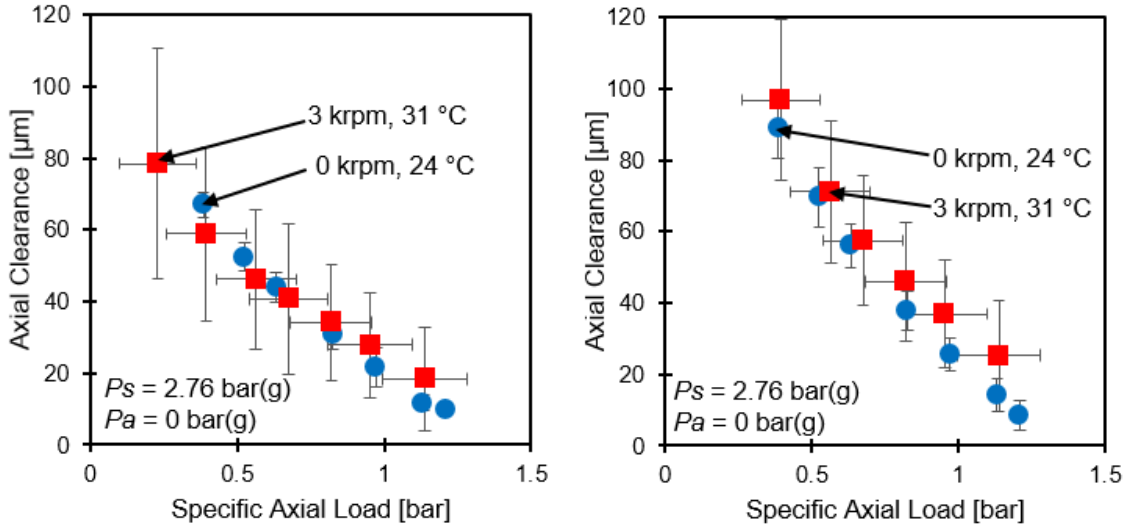

Test Thrust Bearing, P_S = 2.76 bar(g) **Slave Thrust Bearing, P_S = 2.76 bar(g)**

Figure 13. Estimated axial clearance at the center of (left) test and (right) slave thrust bearings vs. specific load (*W/A*) for operation with water at a supply pressure (P_S) of 2.76, 3.45, and 4.14 bar(g) into the thrust bearing. Water is 24 °C and 31 °C as shaft rotates at 0 and 3 krpm, respectively. Water at 3.45 bar(g) feeds the journal bearings. Ambient pressure (P_a) is 0 bar(g). Horizontal error bars represent the uncertainty in the axial load at a 95% confidence level. Vertical error bars indicate the maximum and minimum clearances on the face of the thrust bearing.

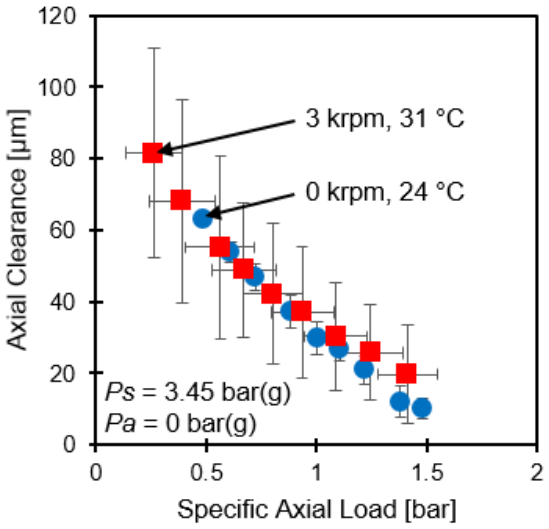

Test Thrust Bearing, P_S = 3.45 bar(g)

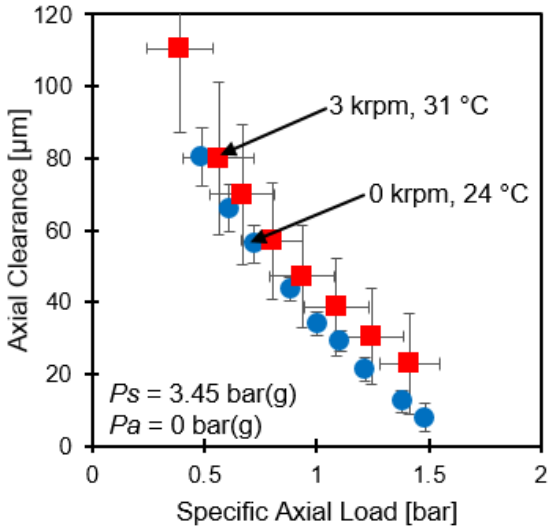

Slave Thrust Bearing, P_S = 3.45 bar(g)

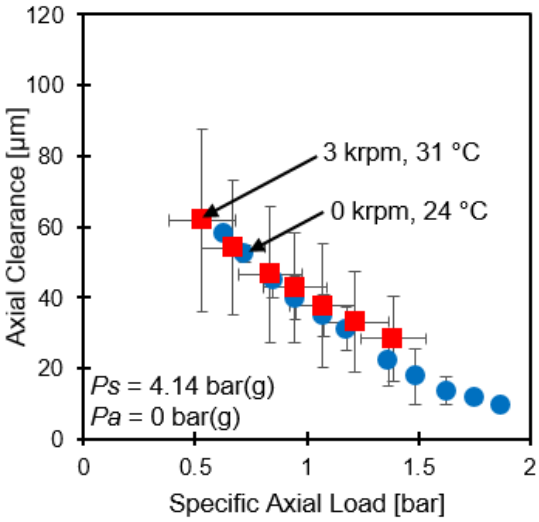

Test Thrust Bearing, P_S = 4.14 bar(g)

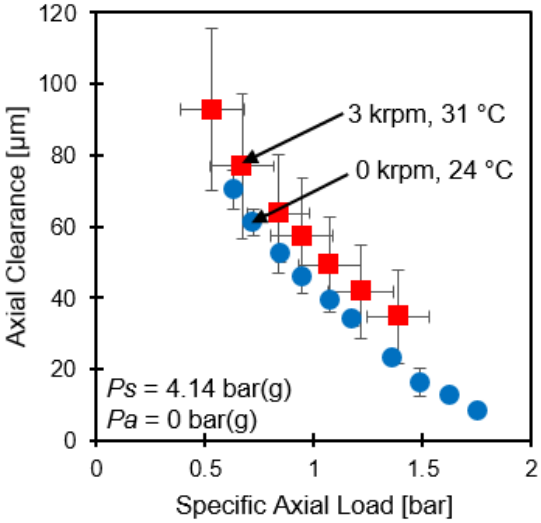

Slave Thrust Bearing, P_S = 4.14 bar(g)

Figure 13. Continued.

For operation at a shaft speed of 3 krpm, Figures 14-17 show the flow rate supplying the test thrust bearing (Q_S), the flow rate exhausting through the inner diameter of the test thrust bearing (Q_{ID}), the ratio of the flow exhausting from the inner diameter to the flow supplying the test thrust bearing (Q_{ID}/Q_S), and the recess pressure ratio (P_R/P_S) versus axial clearance at the center of the test thrust bearing, respectively, for operation with water at 2.76, 3.45, and 4.14 bar(g) supplying the thrust bearing. Note Figure 16 also shows the

ratio of the flow exhausting from the inner diameter to the flow supplying the test thrust bearing (Q_{ID}/Q_S) versus specific axial load (W/A).

At a constant axial clearance (C_0), the flow rate supplying the thrust bearing and exhausting through the inner diameter of the thrust bearing increase as the water lubricant supply pressure increases. However, the magnitude of the water supply pressure does not affect the ratio of flow exhausting through the inner diameter to the flow supplying the thrust bearing. At each water lubricant supply pressure, the flow rate supplying the thrust bearing and the flow rate exhausting though the inner diameter of the thrust bearing decrease as the axial clearance decreases because of the increased flow resistance across the (smaller thin) film lands of the thrust bearing. In addition, the ratio of flow exhausting through the inner diameter to the supply flow is fairly constant (~40%), decreasing slightly as the axial load increases (axial clearance decreases). A decrease in the flow rate causes a lower pressure drop across each orifice, resulting in higher pocket pressures at low axial clearance. At a constant axial clearance, the magnitude of the water supply pressure does not have a large influence on the recess pressure ratio while water supplies the bearing at 2.76-4.14 bar(g).

Figure 18 shows the radial Reynolds number of the flow exhausting from the inner and outer diameter of the thrust bearing versus axial clearance at the center of the test thrust bearing, respectively, for operation with water at 2.76, 3.45, and 4.14 bar(g) supplying the thrust bearings with the rotor spinning at 3 krpm. The radial Reynolds number of the radial flow through the inner diameter (Re_{ID}) is

$$Re_{ID} = \frac{\rho Q_{ID}}{\pi \mu D_{in}} \tag{3}$$

where Q_{ID} is the flow rate exhausting the thrust bearing through the inner diameter. The radial Reynolds number of the radial flow through the outer diameter (Re_{OD}) is

$$Re_{OD} = \frac{\rho Q_{OD}}{\pi \mu D_{out}} \tag{4}$$

where $Q_{OD} = (Q_S - Q_{ID})$. Figure 18 indicates that the radial flow is laminar through the inner and outer diameters for operation at each water supply pressure and axial load. For

operation at 3 krpm, the Reynolds number of the flow in the circumferential direction ($Re = \frac{\rho}{\mu}\omega RC$) at the inner and outer diameters of the test thrust bearing ranges from 160 to 650 and 300 to 1220, respectively, as the clearance increases from 20 um to 80 um, respectively. At a constant axial clearance (constant applied load), Re_{ID} and Re_{OD} increase as the water lubricant supply pressure increases due to the increase in flow rate.

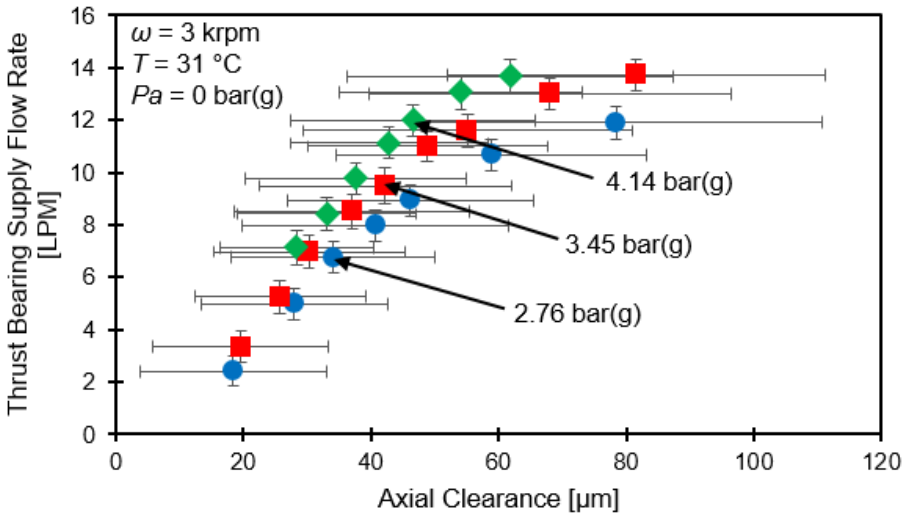

Figure 14. Measured supply flow rate of test thrust bearing vs. axial clearance at center of test thrust bearing for operation with water (31 °C) at a supply pressure (P_S) of 2.76, 3.45, and 4.14 bar(g) into the thrust bearing. Shaft rotates at 3 krpm. Water at 3.45 bar(g) feeds the journal bearings. Ambient pressure (P_a) is 0 bar(g). Vertical error bars represent the uncertainty in the supply flow rate at a 95% confidence level. Horizontal error bars indicate the maximum and minimum clearances on the face of the thrust bearing.

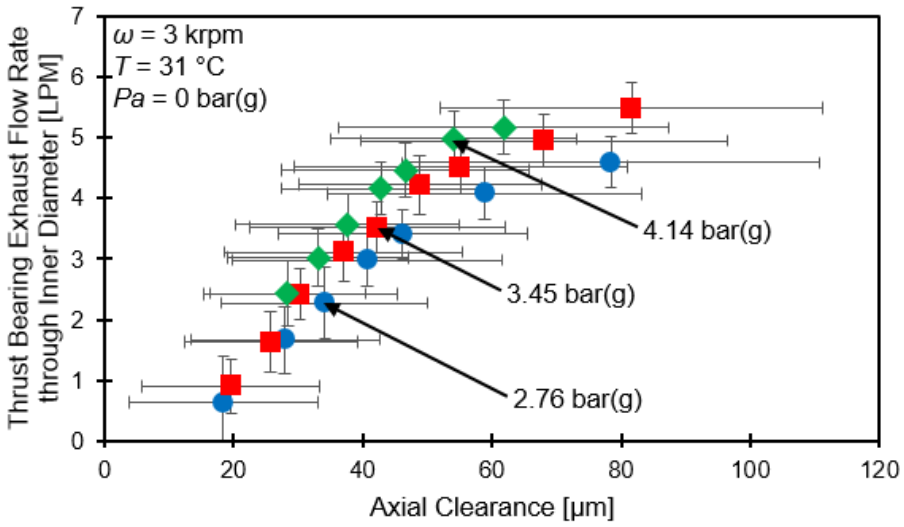

Figure 15. Measured exhaust flow rate through inner diameter of test thrust bearing vs. axial clearance at center of test thrust bearing for operation with water (31 °C) at a supply pressure (P_S) of 2.76, 3.45, and 4.14 bar(g) into the thrust bearing. Shaft rotates at 3 krpm. Water at 3.45 bar(g) feeds the journal bearings. Ambient pressure (P_a) is 0 bar(g). Vertical error bars represent the uncertainty in the flow rate through the inner diameter at a 95% confidence level. Horizontal error bars indicate the maximum and minimum clearances on the face of the thrust bearing.

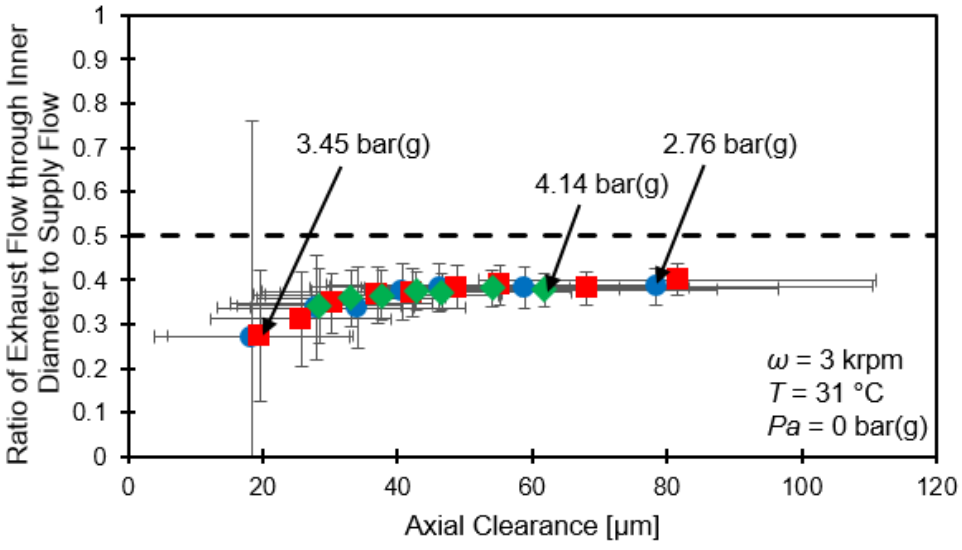

(a)

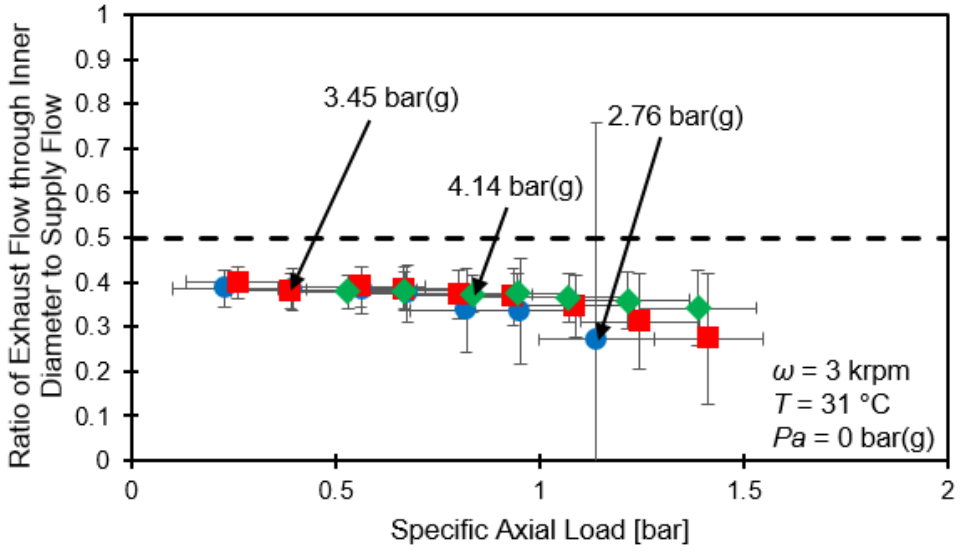

(b)

Figure 16. Ratio of exhaust flow through inner diameter to supply flow to test thrust bearing vs. (a) axial clearance at the center of the test thrust bearing and (b) specific axial load for operation with water (31 °C) at a supply pressure (P_S) of 2.76, 3.45, and 4.14 bar(g) into the thrust bearing. Shaft rotates at 3 krpm. Water at 3.45 bar(g) feeds the journal bearings. Ambient pressure (P_a) is 0 bar(g). Vertical error bars represent the uncertainty in the ratio of exhaust flow through inner diameter to supply flow at a 95% confidence level. Horizontal error bars indicate the maximum and minimum clearances on the face of the thrust bearing and the uncertainty in the specific axial load at a 95% confidence level, respectively.

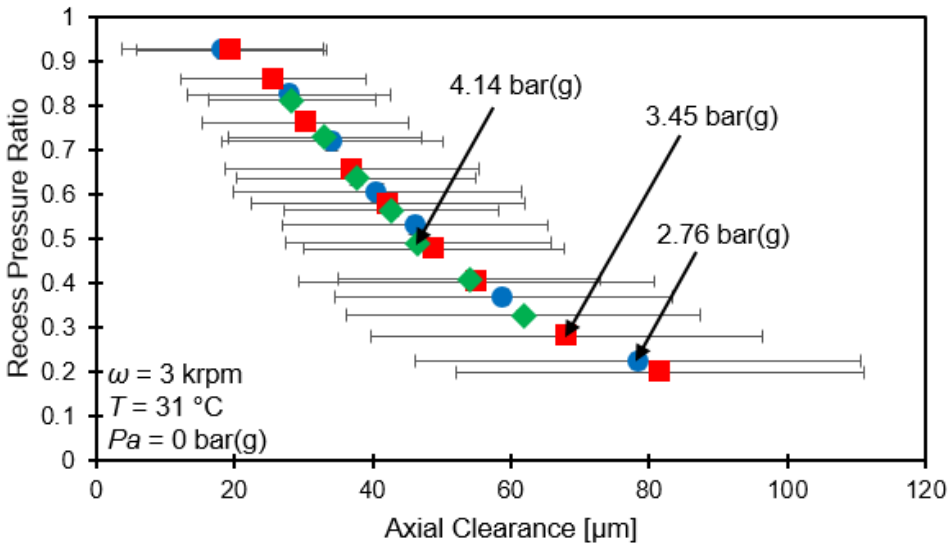

Figure 17. Derived recess pressure ratio (P_R/P_S) of test thrust bearing vs. axial clearance at center of test thrust bearing for operation with water (31 °C) at a supply pressure (P_S) of 2.76, 3.45, and 4.14 bar(g) into the thrust bearing. Shaft rotates at 3 krpm. Water at 3.45 bar(g) feeds the journal bearings. Ambient pressure (P_a) is 0 bar(g). Vertical error bars represent the uncertainty in the recess pressure ratio at a 95% confidence level. Horizontal error bars indicate the maximum and minimum clearances on the face of the thrust bearing.

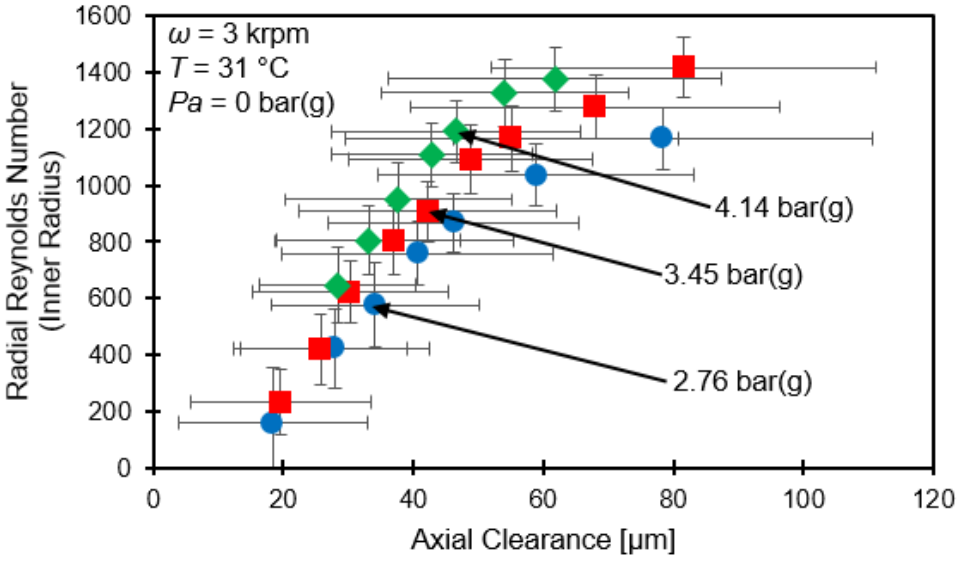

(a) Inner Diameter

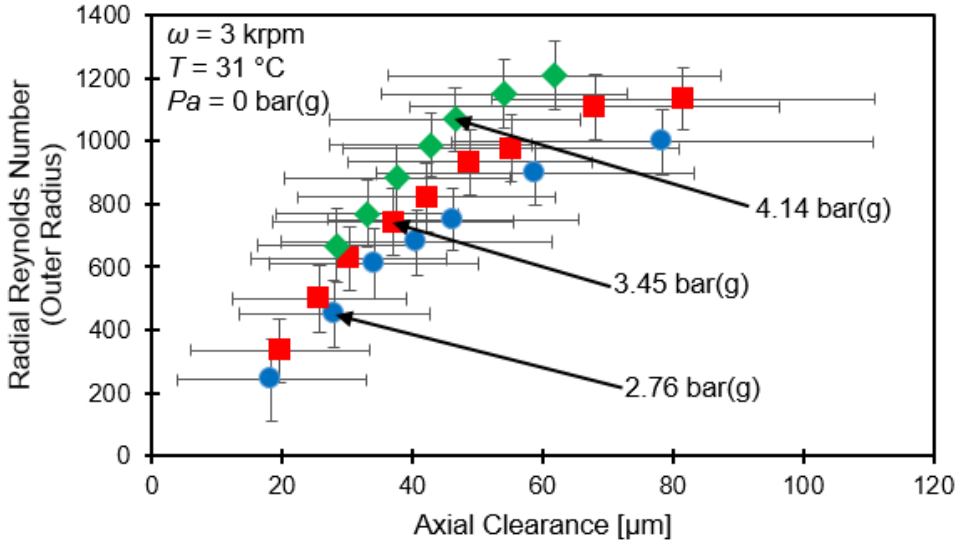

(b) Outer Diameter

Figure 18. Reynolds number of radial flow exhausting through the (a) inner and (b) outer diameter of the test thrust bearing vs. axial clearance at the center of the test thrust bearing for operation with water (31 °C) at a supply pressure (P_S) of 2.76, 3.45, and 4.14 bar(g) into the thrust bearing. Shaft rotates at 3 krpm. Water at 3.45 bar(g) feeds the journal bearings. Ambient pressure (P_a) is 0 bar(g). Vertical error bars represent the uncertainty in the Reynolds number at a 95% confidence level. Horizontal error bars indicate the maximum and minimum clearances on the face of the thrust bearing.

The flow through an orifice ($Q_O = Q_S / N_{pockets}$) is a function of its area (A_O), the pressure drop (P_S - P_R) and fluid density (ρ). From the data, one can obtain an empirical orifice discharge coefficient (C_d), as

$$C_d = \frac{Q_O}{A_O\sqrt{\frac{2}{\rho}(P_S - P_R)}} \tag{4}$$

Note, Eq. (4) assumes the flow rate through all orifices is the same and the pressure in all recess is the same. Figure 19 shows the empirical discharge coefficient (C_d) versus axial clearance at the center of the test thrust bearing for operation with water at 2.76, 3.45, and 4.14 bar(g) supplying the thrust bearings as the rotor spins at 3 krpm. The magnitude of the water lubricant supply pressure does not have a large influence on C_d. However, the axial clearance does affect the orifice discharge coefficient. At a very low axial clearance, C_d is significantly lower and more uncertain than it is at a high axial clearance. As the axial clearance increases from 30 μm to 80 μm, C_d becomes relatively constant (~0.62), as shown in Table 3.

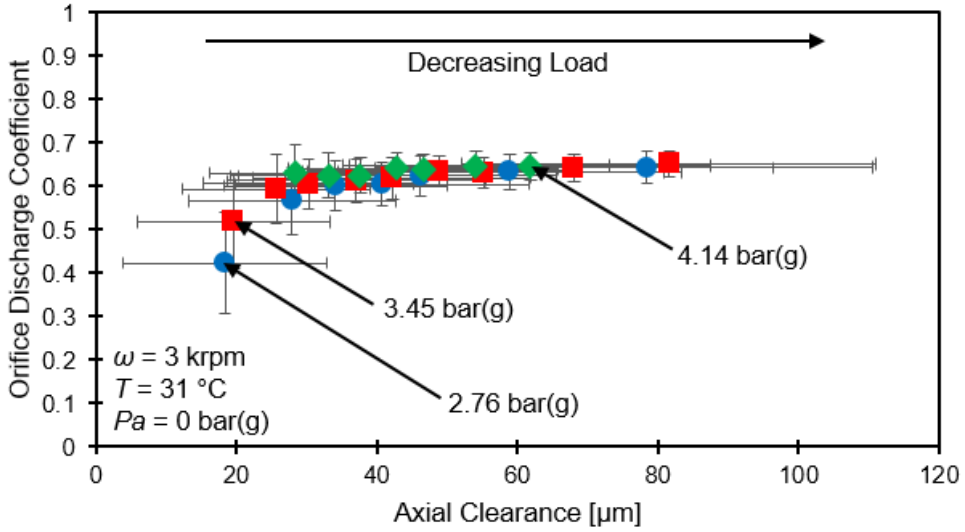

Figure 19. Empirical orifice discharge coefficient (C_d) vs. axial clearance at the center of the test thrust bearing for operation with water (31 °C) at a supply pressure (P_S) of 2.76, 3.45, and 4.14 bar(g) into the thrust bearing. Shaft rotates at 3 krpm. Water at 3.45 bar(g) feeds the journal bearings. Ambient pressure (P_a) is 0 bar(g). Vertical error bars represent the uncertainty in the empirical orifice discharge coefficient at a 95% confidence level. Horizontal error bars indicate the maximum and minimum clearances on the face of the thrust bearing.

Table 3. Estimated orifice discharge coefficient (C_d) for test thrust bearing operating with water (31 °C) at a supply pressure (P_S) of 2.76, 3.45, and 4.14 bar(g). Shaft rotates at 3 krpm. Water at 3.45 bar(g) feeds the journal bearings. Ambient pressure (P_a) is 0 bar(g). Uncertainty in the estimated orifice discharge coefficient is based on a 95% confidence level.

Water Supply Pressure (P_S)	Estimated Orifice Discharge Coefficient (C_d)
2.76 bar(g)	0.61 ± 0.07
3.45 bar(g)	0.62 ± 0.05
4.14 bar(g)	0.64 ± 0.02

Predictions vs. Measured Thrust Bearing Static Load Performance

Using the geometry of the thrust bearing and the average orifice discharge coefficient (C_d) shown above, XLHydroThrust® [9] predicts the bearing performance (C, Q_S, P_R, K) as a function of an applied axial load. Table 8 in Appendix C describes the input data required for XLHydroThrust® [9] as well as the performance parameters that it predicts. Figure 20 shows the predicted axial clearance and estimated axial clearance at the center of the thrust bearing for both the test and slave thrust bearing versus the specific axial load (W/A) for operation with water supplying the thrust bearing at 2.76, 3.45, and 4.14 bar(g) with the rotor spinning at 0 krpm and 3 krpm, respectively. Note that the predictions assume the orifices on the slave thrust bearing have the same discharge coefficient as the orifices on the test thrust bearing. However, there are no measurements for either the flow rate or recess pressure in the slave thrust bearing.

Figures 21-23 depict the measured and predicted thrust bearing supply flow rate, exhaust flow rate through the inner diameter, and the recess pressure ratio (P_R/P_S) versus specific axial load (W/A), respectively, for operation with water (31 °C) supplying the thrust bearings at 2.76, 3.45, and 4.14 bar(g) as the rotor spins at 3 krpm.

The measured and predicted axial clearance (C_0) increase as the water pressure supplied to the thrust bearing increases or the applied axial load decreases. The predicted axial clearance is consistently much larger than the estimated, experimental axial

clearance at the center of the thrust bearing, especially when operating with a high axial load (low axial clearance). However, at a low axial load (high axial clearance), the maximum clearance on the face of the thrust collar is nearly equivalent to the predicted clearance when the rotor spins at 3 krpm. As the applied axial load increases (axial clearance decreases) from its minimum to its maximum magnitude (rotor spins at 3 krpm), the average percent difference in axial clearance increases from 25% to 53%. Thus, as the applied axial load increases (axial clearance decreases), the difference between the predicted and estimated axial clearances becomes more significant.

As the applied axial load decreases and the axial clearance increases, the flow resistance across the film land decreases resulting in a higher supply flow rate and a higher exhaust flow rate through the inner diameter of the thrust bearing for a constant water supply pressure. As the flow rate supplied to the thrust bearing increases, the flow experiences a larger pressure drop through the orifice resulting in a lower recess pressure. As the water pressure supplied to the thrust bearing increases at a constant applied axial load, the flow rate supplying the thrust bearing and exhausting through the inner diameter of the thrust bearing also increases, causing the recess pressure to decrease. The predictions accurately show the influence of the water supply pressure and specific axial load on the supply flow rate, the exhaust flow rate through the inner diameter, and the recess pressure ratio.

The predicted magnitudes of the thrust bearing supply flow rate, exhaust flow rate through the inner diameter, and recess pressure ratio versus specific axial load correlate well with the corresponding measured values at a low specific load (large axial clearance). However, the predicted magnitudes do not correlate well at a high specific load (low axial clearance). As the load increases from its minimum to maximum load (axial clearance decreases) at each supply pressure (rotor spins at 3 krpm), the average percent difference between the predicted and measured supply flow rate, flow rate through the inner diameter, and recess pressure ratio increases from 2% to 47%, 7% to 73%, and 7% to 18%, respectively.

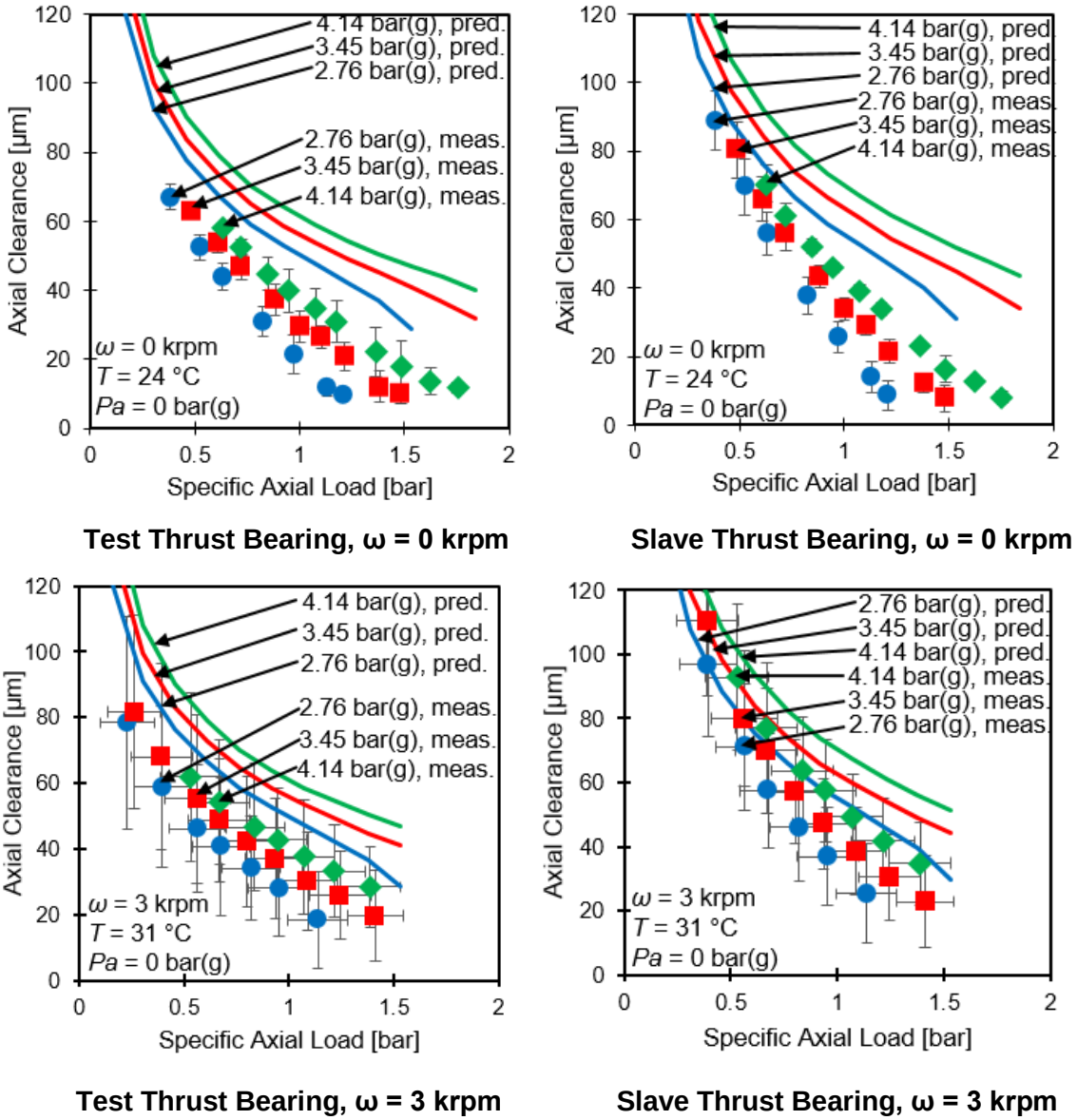

Figure 20. Measured and predicted axial clearance at center of (left) test thrust bearing and (right) slave thrust bearing vs. specific load (*W/A*) for operation with water at a supply pressure (P_S) of 2.76, 3.45, and 4.14 bar(g) into the thrust bearing. Shaft rotates at (top) 0 krpm and (bottom) 3 krpm. Water at 3.45 bar(g) feeds the journal bearings. Ambient pressure (P_a) is 0 bar(g). Horizontal error bars represent the uncertainty in the specific axial load at a 95% confidence level. Vertical error bars indicate the maximum and minimum clearances on the face of the thrust bearing.

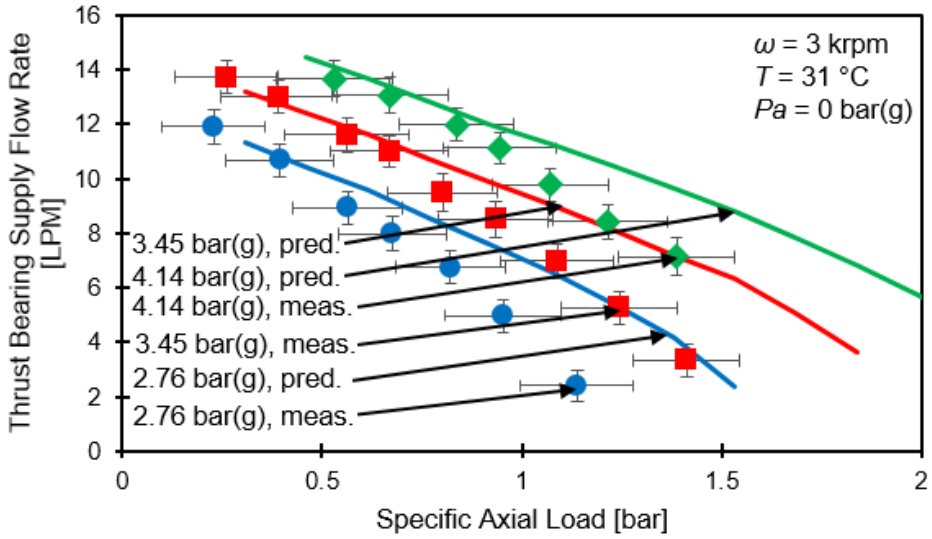

Figure 21. Measured and predicted thrust bearing supply flow rate vs. specific axial load for operation with water (31 °C) at a supply pressure (P_S) of 2.76, 3.45, and 4.14 bar(g) into the thrust bearing. Shaft rotates at 3 krpm. Water at 3.45 bar(g) feeds the journal bearings. Ambient pressure (P_a) is 0 bar(g). Vertical and horizontal error bars represent the uncertainty in the supply flow rate and the specific axial load at a 95% confidence level, respectively.

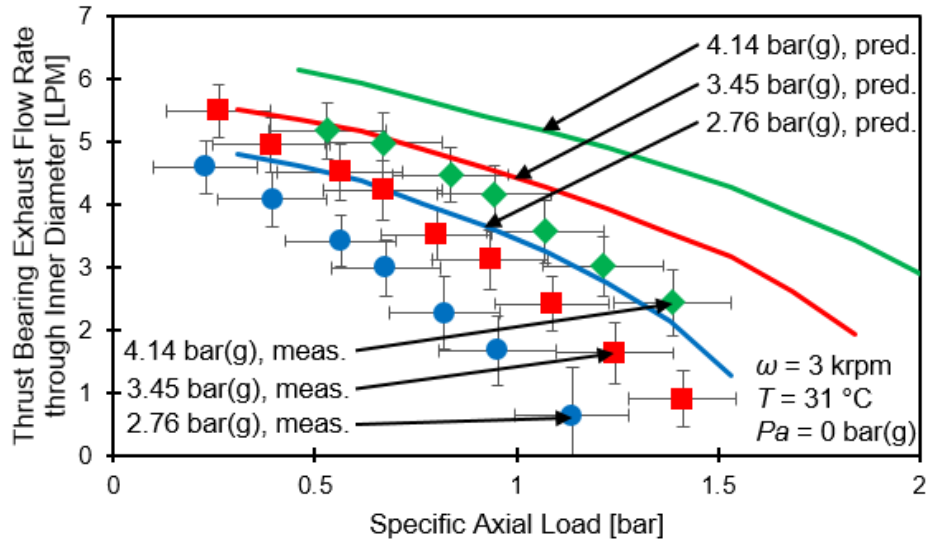

Figure 22. Measured and predicted thrust bearing flow rate through inner diameter vs. specific axial load for operation with water (31 °C) at a supply pressure (P_S) of 2.75, 3.45, and 4.14 bar(g) into the thrust bearing. Shaft rotates at 3 krpm. Water at 3.45 bar(g) feeds the journal bearings. Ambient pressure (P_a) is 0 bar(g). Vertical and horizontal error bars represent the uncertainty in the exhaust flow rate through the inner diameter and the uncertainty in the specific axial load at a 95% confidence level, respectively.

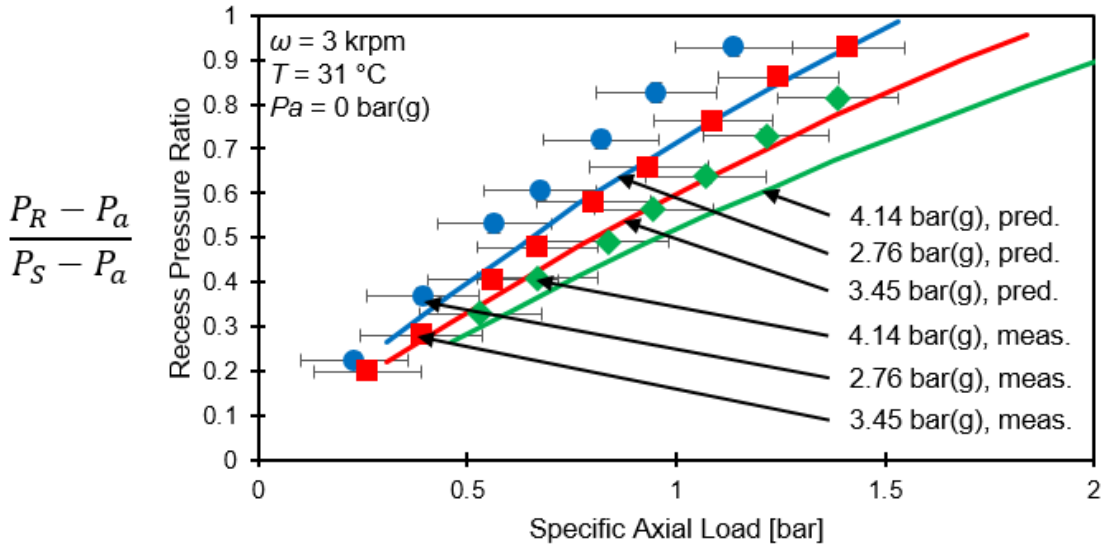

Figure 23. Measured and predicted recess pressure ratio vs. specific axial load for operation with water (31 °C) at a supply pressure (P_S) of 2.76, 3.45, and 4.14 bar(g) into the thrust bearing. Shaft rotates at 3 krpm. Water at 3.45 bar(g) feeds the journal bearings. Ambient pressure (P_a) is 0 bar(g). Vertical and horizontal error bars represent the uncertainty in the recess pressure ratio and the specific axial load at a 95% confidence level, respectively.

For tests with rotor speed, Figure 24 shows the measured axial load versus clearance (C_0) and an exponential curve fit (its functional derivative provides an estimate of the TB static stiffness). Figure 25 shows the derived TB static stiffness (K) versus axial clearance (C_0) for operation with water (31 °C) supplying the thrust bearing at 2.76, 3.45, and 4.14 bar(g). At a constant axial clearance, the axial stiffness and the load capacity increase as the water pressure supply increases. With a constant water lubricant supply pressure, the load capacity and axial stiffness decrease as the axial clearance increases.

As the clearance continues to increase, the load capacity and axial stiffness decrease. The estimated axial stiffness (K) is on the same order of magnitude as the predicted axial stiffness. However, K shows a higher magnitude at a lower axial clearance than the predicted axial stiffness. Note that K in Figure 25 is only valid for the range of clearances shown and cannot be extrapolated to any higher or lower axial clearance

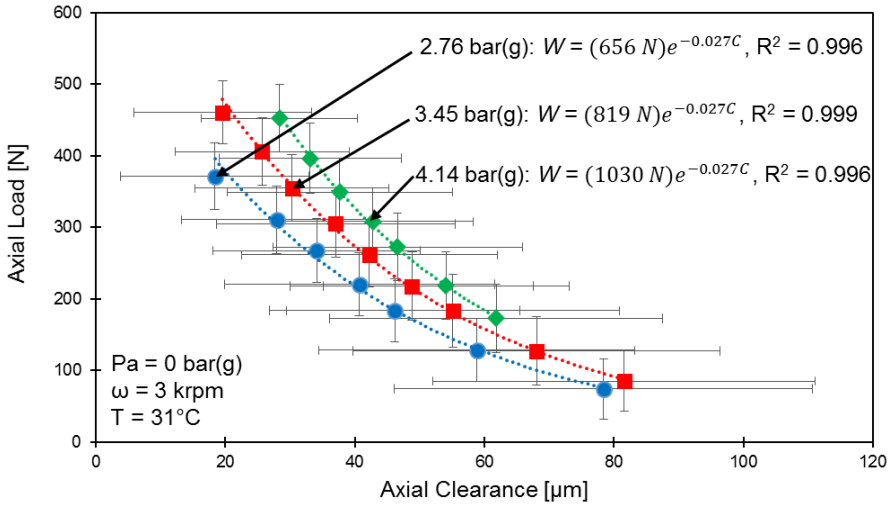

Figure 24. Measured axial load vs. axial clearance at the center of the test thrust bearing with exponential curve fit ([*C*]=μm, [*W*]=N) for operation with water (31 °C) at a supply pressure (P_S) of 2.76, 3.45, and 4.14 bar(g) into the thrust bearings. Shaft rotates at 3 krpm. Water at 3.45 bar(g) feeds the journal bearings. Ambient pressure (P_a) is 0 bar(g). Vertical error bars represent the uncertainty in the axial load at a 95% confidence level. Horizontal error bars indicate the maximum and minimum clearances on the face of the thrust bearing.

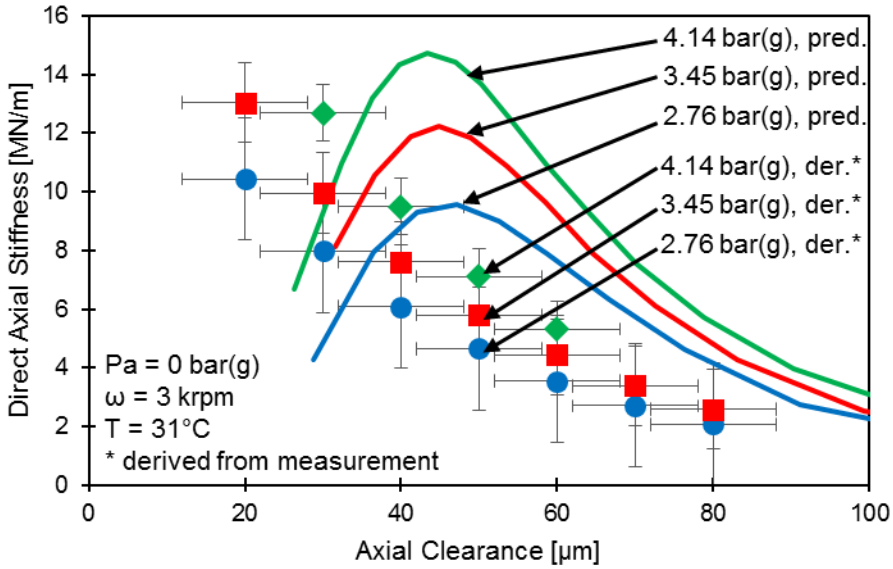

Figure 25. Derived and predicted axial stiffness vs. axial clearance at the center of the test thrust bearing for operation with water (31 °C) at a supply pressure (P_S) of 2.76, 3.45, and 4.14 bar(g) into the thrust bearings. Shaft rotates at 3 krpm. Water at 3.45 bar(g) feeds the journal bearings. Ambient pressure (P_a) is 0 bar(g). Estimated axial stiffness derived from exponential curve fit (shown in Figure 24). Vertical and horizontal error bars represent the uncertainty in the axial stiffness and the axial clearance at the center of the test thrust bearing at a 95% confidence level, respectively.

Conclusion

A water lubricated test rig is functional to provide test data to validate model predictions towards improving the design of thrust bearings. Previously, measurements on the same test rig showed good correlation with predictions for water lubricated hybrid thrust bearings [3].

For operation at a low shaft speed (3 krpm), water at room temperature (24 °C and 31 °C) feeds the journal bearings at 3.45 bar(g) and the thrust bearings at increasing supply pressure (max. 4.14 bar(g)). At each water lubricant supply pressure into the thrust bearings, the test thrust bearing applies a decreasing load onto the rotor thrust collar. At a constant axial load, the axial clearance, the supply flow rate, and the central exhaust flow rate increase as the pressure of the water supplying the thrust bearing increases. However, the axial load per unit area [$A = \frac{\pi}{4}(D_{out}^2 - D_{in}^2)$] is a fraction of the supply pressure (P_S) to thrust bearings because the recess area is only a fraction of the load bearing area. At a constant supply pressure (P_S), the axial clearance (C) decreases as the axial load (W) increases. The reduced clearance causes an increased flow resistance across the film lands of the thrust bearing, ultimately amounting to a reduced flow rate at a high axial load (low axial clearance). As the flow rate decreases, the pressure drop across the orifice also decreases, which results in higher recess pressures. Therefore, as the axial load increases (axial clearance decreases) with a constant water lubricant supply pressure, the supply flow rate and the flow rate through the inner diameter decrease as the recess pressure ratio increases. In addition, as the TB axial clearance decreases or the water supply pressure increases, the TB axial load and stiffness increase. Overall, the measurements show repeatable results.

XLHydroThrust® [9] used the TB geometry to deliver predictions of bearing performance. The predictions and measurements qualitatively agree on how the water supply pressure/axial load affect the bearing performance. However, there are discrepancies between the predicted and measured magnitudes at a high axial load (small axial clearance). At the lowest axial load for each water supply pressure administered to

the test thrust bearing (3 krpm), the average percent difference between the predicted and measured supply flow rate, flow rate through inner diameter, axial clearance, and the recess pressure ratio is 2%, 7%, 25%, and 18%, respectively. At the highest axial load for each water supply pressure on the test thrust bearing (3 krpm), the average percent difference between the predicted and measured supply flow rate, flow rate through inner diameter, axial clearance, and recess pressure ratio is 47%, 73%, 53%, and 18%, respectively. The discrepancy (static and dynamic) at a low axial clearance (high load) is caused by the large misalignment of the thrust collar.

Lastly, Appendices A and B detail the construction of a water pump delivery system and a procedure to extract axial force coefficients from impact load tests, respectively.

Future work will measure the performance of a hybrid thrust bearing (eight pocket) lubricated with water. The test rig could also be used to test other thrust bearings with a 3.0 inch outer diameter at speeds up to 9 krpm ($\omega R_{out} = 35.9$ m/s). The first task will be to measure the axial response from an impact load over a range of rotor speed (max. 9 krpm), bearing supply pressure (max. 10 bar), thrust bearing clearance (min. 20 μm). The second task is to estimate the thrust bearing stiffness and damping coefficients. Impact loads delivered through an ad-hoc mechanism presently under troubleshooting

References

[1] Rohmer, M., Wilkinson, S. and San Andrés, L., 2015, "Revamping and Preliminary Operation of a Thrust Bearing Test Rig," Annual Progress Report to the Turbomachinery Research Consortium, TRC-B&C-03-2015, Turbomachinery Laboratory, Texas A&M University, College Station, TX, May.

[2] San Andrés, L., 2013, "A Test Rig for Evaluation of Thrust Bearings and Face Seals," Proposal to the Turbomachinery Research Consortium, Turbomachinery Laboratory, Texas A&M University, College Station, TX, May.

[3] Forsberg, M., 2008, "Comparison Between Predictions and Experimental Measurements for an Eight Pocket Annular HTB," M.S. Thesis, Mechanical Engineering, Texas A&M University, College Station, TX.

[4] Esser, P., 2010, "Measurements versus Predictions for a Hybrid (Hydrostatic plus Hydrodynamic) Thrust Bearing for a Range of Orifice Diameters," M.S. Thesis, Mechanical Engineering, Texas A&M University, College Station, TX.

[5] San Andrés, L., 2010, *Modern Lubrication Theory*, "Hydrostatic Journal Bearings," Notes 12b, Texas A&M University Digital Libraries, http://repository.tamu.edu/handle/1969.1/93197.

[6] Rowe, W., 1983, *Hydrostatic and Hybrid Bearing Design*, Textbook, Butterworths, London, England, pp. 1-20, 46-68.

[7] Sternlicht, B. and Elwell, R.C., 1960, "Theoretical and Experimental Analysis of Hydrostatic Thrust Bearings," ASME J. Basic Eng., **82**(3), pp. 505-512.

[8] San Andrés, L., 2000, "Bulk-Flow Analysis of Hybrid Thrust Bearings for Process Fluid Applications," ASME J. of Trib., **122**(1), pp. 170-180.

[9] San Andrés, L., 2002, "Effects of Misalignment on Turbulent Flow Hybrid Thrust Bearings," ASME J. of Trib., **124**(1), pp. 212-219.

[10] San Andrés, L., Phillips, S., and Childs, D., 2008, "Static Load Performance of a Hybrid Thrust Bearing: Measurement and Validation of Predictive Tool," 6th Modeling and Simulation Subcommittee / 4th Liquid Propulsion Subcommittee / 3rd Spacecraft Propulsion Subcommittee Joint Meeting. December 8-12, Orlando, Florida, JANNAF-120 Paper.

[11] Ramirez, F., 2008, "Comparison between Predictions and Measurements of Performance Characteristics for an Eight Pocket Hybrid (Combination Hydrostatic/Hydrodynamic) Thrust Bearing," M.S. Thesis, Mechanical Engineering, Texas A&M University, College Station, TX.

[12] XLTRC^2, 2002, Computational Rotordynamics Software Suite, Turbomachinery Laboratory, Texas A&M University, College Station, TX.

[13] San Andrés, L. and Childs, D., 1997, "Angled Injection – Hydrostatic Bearings, Analysis and Comparison to Test Results," ASME J. Tribol., **119**, pp. 179-187.

[14] San Andrés, L., Rohmer, M., and Park, S., 2015, "Failure of a Test Rig Operating with Pressurized Gas Bearings: A Lesson on Humility," ASME paper GT2015-42556.

[15] Coleman, H. and Steel, W., 1989, *Experimentation and Uncertainty Analysis for Engineers*, Textbook, John Wiley and Sons, Inc., New York, NY, pp. 1-71.

Appendix A: Closed Loop Water Supply System

Figure 26 presents a schematic diagram of a closed loop water supply system for the thrust bearing test rig. Prior operation* [A1] sourced water from the test facility central water system and discarded it after passing through the test rig. The objective of the new closed loop water supply system is to reach a higher bearing supply pressure (more than 150 psig) and a higher flow rate (25 GPM).

The system, built in 2015 and completed in January 2016, implements a closed loop by recycling water supplied to the lubricated radial and thrust bearings. Figures 27 and 28 display photographs of the system hardware (main pump, return pump, and heat exchanger) and pump shed with reservoir tank, respectively. As shown in Figure 26, the system utilizes a single, 7.5 HP, constant speed multi-stage vertical turbine pump to deliver water at 222 psig pressure and maximum 25 GPM flow rate to the test rig. The system includes a 2 HP, self-priming return pump for recirculation of water, an air-cooled heat exchanger to prevent excessive high temperature of water, a 500 gallon capacity reservoir tank as well as a host of valves and gauges to control and monitor flow performance. The pump shed (located outside of the test-cell) accommodates the system hardware for protection from the environment.

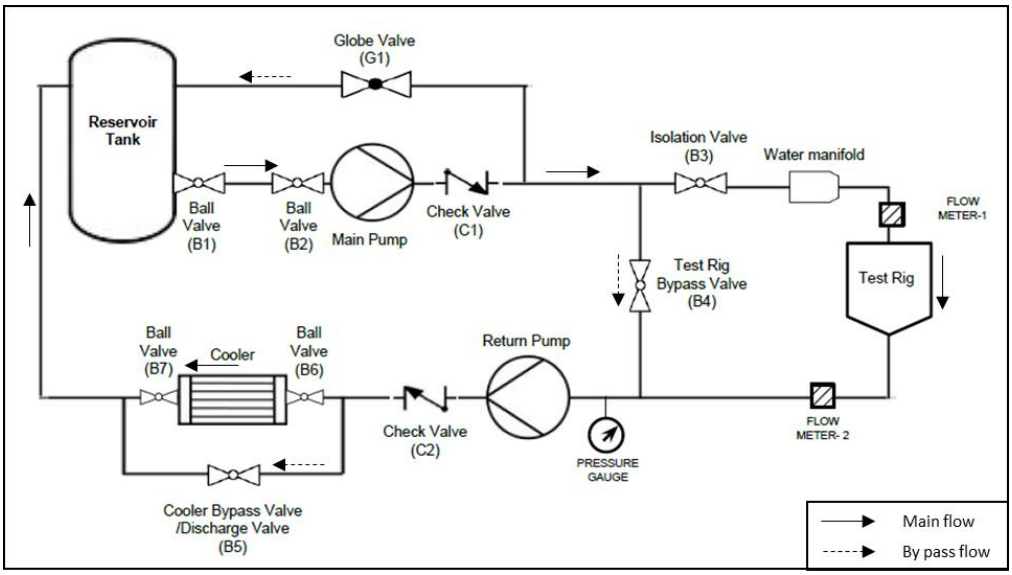

Figure 26. Schematic diagram of closed loop water supply system for thrust bearing test-rig (2015).

*Additional references at end of appendix

Figure 27. Photograph of vertical main pump (left), centrifugal return pump (middle), and heat exchanger (right) installed outside of test-cell.

Figure 28. Reservoir tank (left) and pump shed (right) accommodating two pumps and heat exchanger located outside of test-cell.

Figure 4 shows the performance curve for the main pump. The pump has 17 stages which generates a head up to 513 feet (222 psig) with 25 GPM flow rate at the operating

point. The pump requires a net positive suction head (NPSH) of 3.4 feet. This is achieved by a minimum level of water (300 gallons) in the reservoir tank. The pump efficiency is 68 % at the operating point as seen in Figure 29. The main pump enables high supply pressure (max. 150 psig) to the bearings when compared to the previous arrangement (max. 60 psi). Figure 30 shows the return pump performance curve (marked as 'D'). The return pump discharges water up to a head of 85 feet (37 psig) at 25 GPM flow rate as shown by the operating point in Figure 5. The pump discharge head capacity is up to 100 feet for a flow rate lower than 25 GPM.

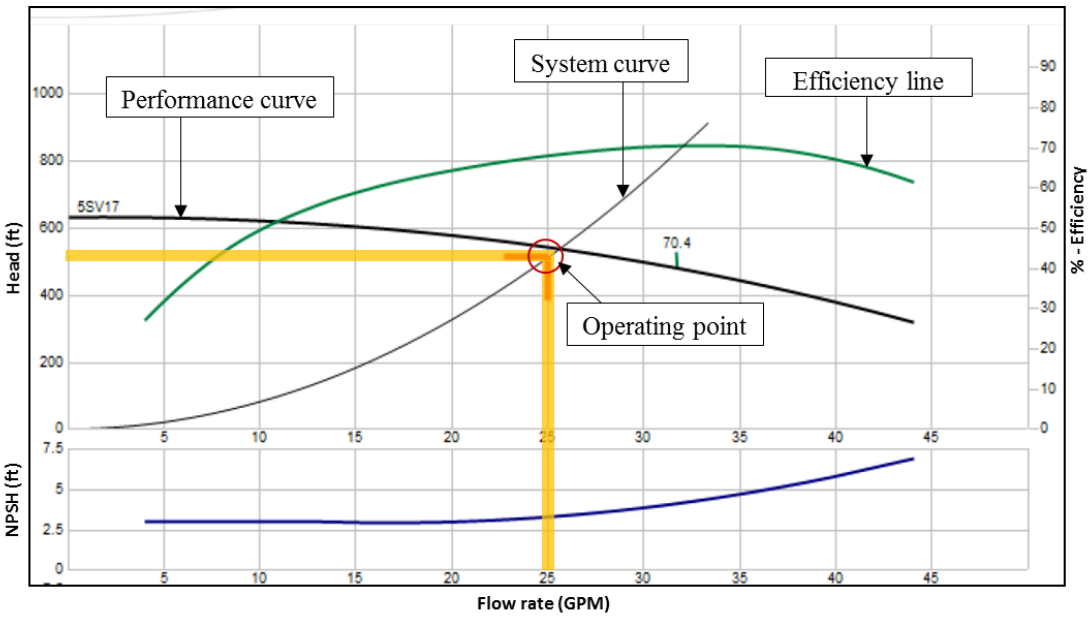

Figure 29. Main pump performance curve. (Source: Goulds's product manual)

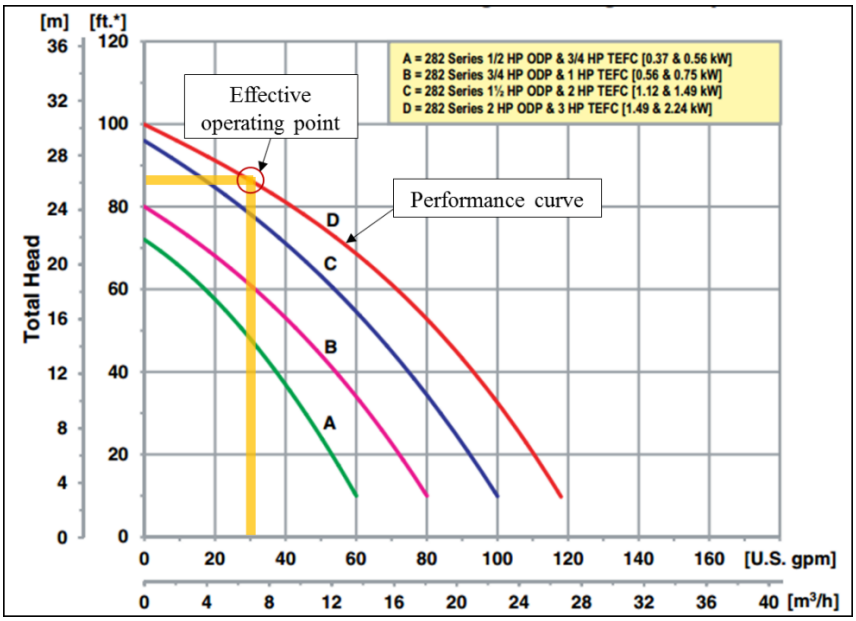

Figure 30. Return pump performance curve. (Source: AMT's product manual)

Additionally, the system utilizes deionized water to prevent corrosion of the bearing and rotor surfaces. A deionization (DI) plant shown in Figure 31 makes up for the deionized water lost due to intermittent leakage through the test rig. The deionization plant has five stages of filtration method. First, water passes through a sediment pre-filter to remove sand, dust, etc., that would otherwise clog the upcoming carbon filter. The carbon block pre-filter removes organics and chlorine from the water. The next stage of the system is the Reverse Osmosis (RO) membrane. Water pressure (80 psig) available from domestic supply system is used to force the water through the semipermeable RO membrane. The membrane only allows the pure water molecules to pass through it while most (inorganic) salts, micro-organisms and high molecular weight organics in the water are rejected by the membrane and drained. Furthermore, the DI plant has two stages of deionization that polish the RO water to less than one ppm (part per million) purity. Two TDS (Total Dissolved Solids) meters monitor every step in the purification process. An Automatic Flush System periodically drains accumulated impurities and concentrated waste water from the surface of the RO membrane to help increase the life of the membrane. A TDS meter at the outlet of the DI plant displays a reading of zero ppm while in operation,

otherwise the DI cartridge should be replaced (regardless, the cartridge should be replaced every 6 months as a precaution).

Figure 31. Photograph of deionization (DI) plant generating 180 gallons/day of deionized water. (Source: Spectrapure product catalog)

Figure 27 shows an air-cooled heat exchanger to control the water temperature. The fin-cooled heat exchanger has a maximum operating pressure of 300 psig and maximum operating temperature of 350 °F. Thermal analysis by considering the rotor operating at 10 krpm and water supply of 150 psig indicate that the temperature of water in the reservoir tank would increase at a rate of 1.3 °F/hour. For short running times, low rotor speed (less than 10 krpm), or operation with a low outside temperature (less than 85°F), the water temperature increase is not significant and the heat exchanger is bypassed. Moreover, heat loss in the lubricant due to heat transfer in a pipe also reduces the water temperature.

Figure 32 shows the predicted heat transfer and pressure drop in different heat exchanger manufactured by Hayden Inc. for oil with 50 SSU viscosity. Curve #6 shown in Figure 32 represents the cooler used in the water supply system. Figure 33(a) shows the predicted pressure drop vs. flow rate for the heat exchanger operating with 50 SSU oil. Using linear curve fit, the extrapolated pressure drop is 37 psig at 25 GPM flow. However, water at room temperature has a viscosity of 31 SSU, which results in a lower pressure drop. The vendor provided a pressure drop multiplier to account for different viscosity fluid. Figure 33(b) shows a pressure drop multiplier vs. the viscosity of the working fluid. Using a parabolic curve fit, the extrapolated pressure drop multiplier of 0.73 corresponds

to 31 SSU. This results in a pressure drop of 27 psig or 62 feet of head loss, which accounts for 83% of the head loss between the test rig and the reservoir tank.

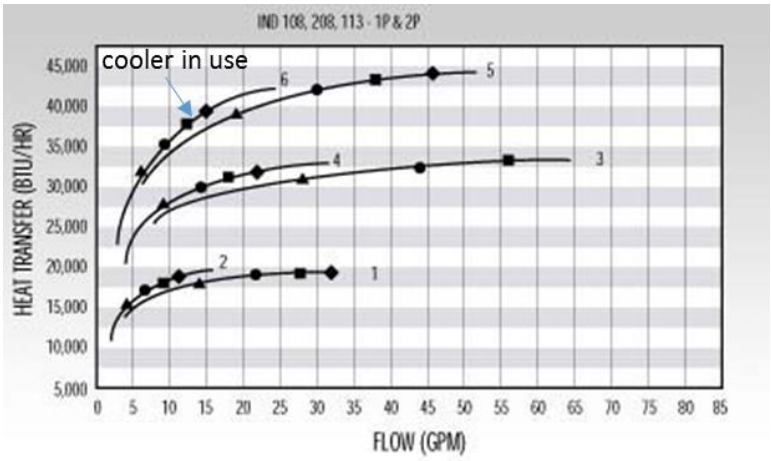

Figure 32. Predicted pressure drop and heat transfer vs. flow rate in various coolers for oil with 50 SSU viscosity. Triangle, circle, square, and diamond represent 5, 10, 15, and 20 psi pressure drop. (Source: Hayden Inc. product manual)

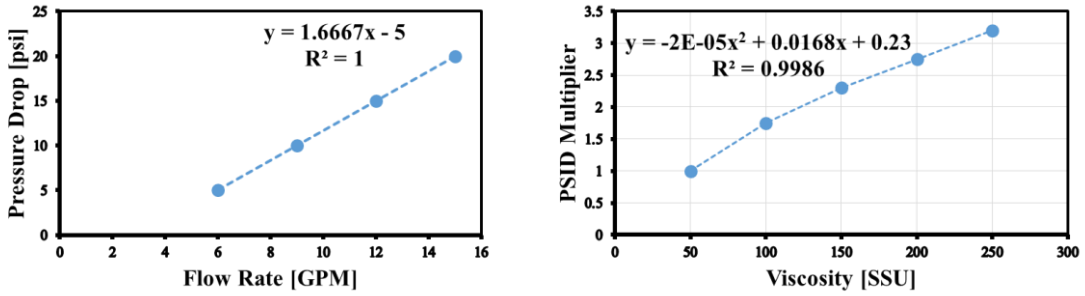

(a) (b)

Figure 33. (a) Predicted pressure drop vs. flow rate in heat exchanger for oil with 50 SSU viscosity. Linear curve fit shown. (b) Predicted pressure drop multiplier vs. viscosity of working fluid in cooler. Quadratic curve fit shown.

Figure 34 show photographs of the steel and PVC (poly vinyl chloride) piping arrangement for the system. Schedule 40, 1-1/4" galvanized steel piping with an overall length of approximately 30 feet connects the main pump (outside of the test-cell) to the rig. Schedule 40, 1-1/4" to 2" PVC piping with an overall length of roughly 50 feet runs from the rig outlet to the reservoir tank via a return pump and heat exchanger. A 20µm sediment filter installed before the test-rig prevents debris from entering the bearing.

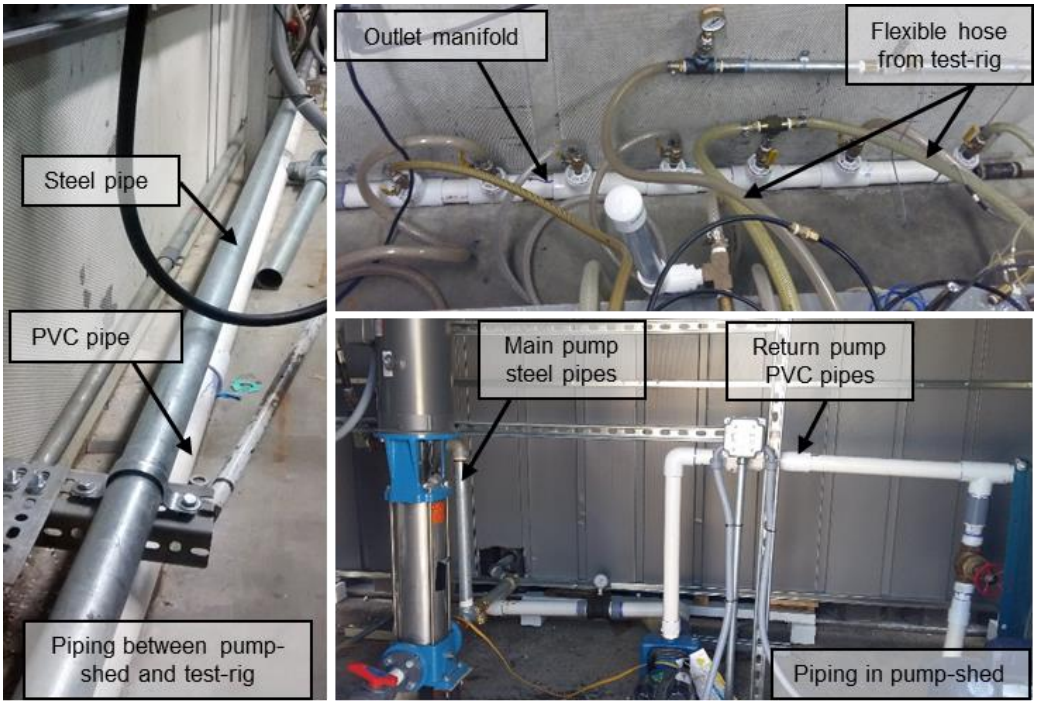

Figure 34. Piping arrangement from pump-shed to test-rig and vice-versa for the water supply system of test-rig.

Table 4 details the total cost (not including labor) incurred to build this system. After procurement of all major components listed in Table 4, installation of the entire system required three months. Later, system testing and commissioning required one month to achieve efficient operation. The water supply system requires the simultaneous operation of two pumps, namely the main pump to supply water to test rig, and the return pump to deliver water back to the reservoir tank. Balance of operation between both the pumps ensures leakage-free functioning of the test-rig. Two operating conditions cause unbalanced operation between both the pumps. In the first case, the main pump discharges more flow to the return pump than its capacity. This will cause the excess water to leak out through the rig. In the second case, the main pump discharges lesser flow to the return pump than it capacity. Due to lack of flow, the return pump undergoes cavitation (suction of air) which could cause damage to impeller and pump housing. This will also cause leakage of water through the rig due to loss of suction by the return pump.

Turbine type flow meters at the inlet and outlet of the test-rig measure the flow rate, providing the feedback required to manually balance the pumps. A globe valve “G1” as

shown in Figure 26 by diverting excess flow back to the reservoir tank sets the flow going to the test-rig. Ball valves “B5” and “B6” as shown in Figure 26 controls the flow from the discharge of the return pump to the reservoir tank via heat exchanger or by-pass line. Throttling of these valves ensures continuous flooded operation of the return pump (without cavitation) and maintains water flow balance between the two pumps.

Students completed installation and testing of the closed loop water supply system in January, 2016.

Table 4. Components and cost of parts of closed loop water supply system.

Components	**Cost ($)**
Main pump	1975
Return pump	596
Reservoir tank	475
Heat exchanger (in-house)	-
Deionizing plant & filters	494
Electrical wiring	3271
Piping and fittings	1765
Miscellaneous	363
Total system cost	**$ 8,939**

Head Loss Analysis of Closed Loop Water Supply System

Energy loss occurs in the flowing water due to pipe wall friction. This energy loss is stated in terms of head loss (ft.) of the fluid. The Darcy-Weisbach equation to calculate head loss in a pipe is

$$H = f\frac{L}{D}\frac{V^2}{2g} \tag{5}$$

where, H = Head Loss (ft), f = Friction factor related to roughness inside pipe, L = Length of pipe (ft), D = Diameter of pipe (ft), and V = Average liquid velocity in pipe (ft/s).

The head loss equation in the valves and pipe fittings is

$$H = K\frac{V^2}{2g} \tag{6}$$

where K is a flow resistance coefficient (experimentally assigned 'K' factor for each pipe component)

The main pump must deliver water to the bearings at the desired pressure while still incurring head losses on the way. Head loss calculation ensures adequate test conditions (flow and pressure) are met at the test rig location. The following analysis considers a supply of water pressure at 150 psig into each radial and thrust bearing. The thrust bearings have a 3 mil (76μ) axial clearance and require a combined 13.5 GPM of water, while the radial bearings require 9.5 GPM, as predicted by XLHydroTHRUST® [A2] and XLHydroJET® [A3], respectively. The flow rate of 23 GPM (13.5 + 9.5 GPM) gives a 6 ft/s velocity in the main supply pipe. In the head loss analysis, it assumes that the globe valve "G1" directs 23 GPM of flow to the test rig and 2 GPM to the reservoir tank via the bypass line. The flow exiting the test rig is at ambient pressure (zero gauge pressure). Tables 2 and 3 present the calculated total head loss in the pipes from the main pump to the test-rig and from the test-rig to the reservoir tank, respectively.

From the head loss data in Table 5, the main pump must overcome a minimum pressure loss of 32 psig to provide the desired pressure (150 psig) to the test-rig. This demands the generation of a minimum discharge pressure of 182 psig (150 psig + 32 psig) from the main pump. However, it would be appropriate to maintain a safety margin of at least 20% requiring a minimum discharge pressure of 218 psig from the pump. Based on the performance curve of the main pump, it produces a discharge pressure of 222 psig at 25 GPM meeting the requirements needed to achieve the desired conditions (150 psig pressure and 23 GPM flow rate) at the test rig.

Table 5. Head loss from the main pump to the test-rig due to various flow restrictions.

Segment of Flow Path	Restrictive Component	Head Loss to Water Supplied to Each Bearing					
		Slave Thrust Bearing		Radial Bearing		Test Thrust Bearing	
Main Pump to Water Manifold	Pipe			1.0 ft	0.4 psi		
	Elbows			5.0 ft	2.2 psi		
	Tee			2.7 ft	1.2 psi		
	Globe Valve			6.6 ft	2.9 psi		
Total Head Loss				**15.3 ft**	**6.7 psi**		
Water Manifold to Bearings in Test Rig	Pipe	0.6 ft	0.3 psi	0.6 ft	0.3 psi	0.6 ft	0.3 psi
	Tees	21.4 ft	9.3 psi	22.0 ft	9.5 psi	20.5 ft	8.9 psi
	Hose	6.8 ft	2.9 psi	01.6 ft	0.7 psi	01.4 ft	0.6 psi
	Pressure Regulator	16.2 ft	7 psi	23.1 ft	10 psi	34.7 ft	15 psi
Total Head Loss		**45.8 ft**	**19.5 psi**	**47.6 ft**	**20.5 psi**	**58.0 ft**	**24.8 psi**
Combined Total Head Loss ≈		**61 ft**	**26 psi**	**63 ft**	**27 psi**	**73 ft**	**32 psi**

From the head loss data in Table 6, the return pump must be capable of delivering flow to a head of 74 feet. Again, it is appropriate to consider a safety margin of 20% leading to a requirement that the return pump discharge water up to a minimum head of 88 feet at 23 GPM. Based on the performance curve of the return pump, it discharges water to a head of more than 88 feet at flow rate of 23 GPM, meeting the requirement of the system.

Table 6. Head loss from the test rig to the reservoir tank due to various flow restrictions.

Restrictive Component	Head Loss to Water	
Pipe	0.6 ft	0.3 psi
Elbows	4.1 ft	1.8 psi
Tee	0.5 ft	0.3 psi
Check Valves	1.1 ft	0.5 psi
Heat exchanger	61.9 ft	26.8 psi
Reservoir tank head	6 ft	3.5 psi
Total Head Loss ≈	**74 ft**	**32 psi**

The head loss analysis thus reveals that both pumps are sufficient to overcome the friction losses in the pipes and to meet the required test conditions.

References

[A1] Rohmer, M., San Andrés, L., 2015, "Revamping and Preliminary Operation of a Thrust Bearing Test Rig," TAMU Report to TRC, *Turbomachinery Laboratory, Texas A&M University*.

[A2] San Andrés, L., 2002, "Effects of Misalignment on Turbulent Flow Hybrid Thrust Bearings," ASME J. of Trib., **124**(1), pp. 212-219.

[A3] San Andrés, L. and Childs, D., 1997, "Angled Injection – Hydrostatic Bearings, Analysis and Comparison to Test Results," ASME J. Tribol., **119**, pp. 179-187.

Appendix B: Identification of Thrust Bearing Structural Force Coefficients and Preliminary Experimental Results

Identification of Structural Force Coefficients

Thrust bearing force coefficients (stiffness *K*, damping *C*, and added mass *M*) enable the prediction and control of axial rotor motions under dynamic loading. Obtaining reliable estimates of the bearing operating performance in actual test conditions is (although challenging) necessary to reduce the discrepancy between measurements and predictions [B1].

Figure 35 shows a schematic view of the test thrust bearing and load shaft assembly modeled as a one degree of freedom (1-DOF) system [B2]. Let z_{TTB} and z_R be the absolute displacements of the TB and rotor, respectively, and z ($z_{TTB} - z_R$) is the relative displacement between both components. A linear viscous damper (C_{TTB}) and stiffness (K_{TTB}) denote the thrust fluid film bearing.

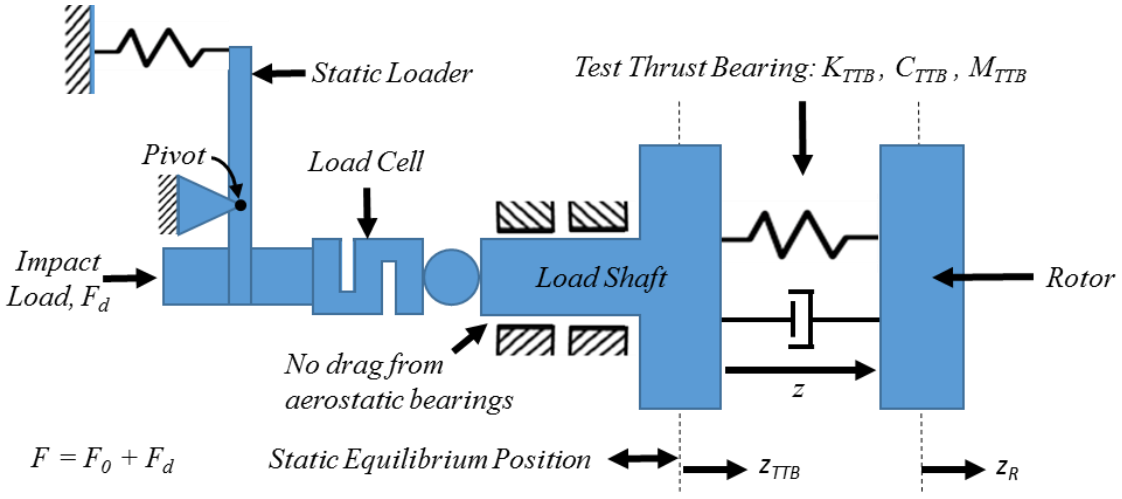

Figure 35. Schematic view of 1-DOF model of test TB for parameter identification.

The instrumentation used during the dynamic tests includes six eddy current sensors (three on each thrust bearing), one piezoelectric accelerometer affixed to the test thrust bearing cartridge along the axial direction, and one load cell mounted on one end of the

static loader. Three eddy current sensors define a plane and enable calculation of the operating clearance at the center of the test TB and slave TB (see Appendix E).

At static equilibrium, the applied load F_0 is balanced by the test TB force, F_{TB_0}, generated by equilibrium clearance $c_o = z_o$.

Due to an impact load ($F_{d(t)}$), the test element (thrust bearing) in Figure 1 undergoes small amplitude motions about its static equilibrium position. The test and slave thrust bearings react to the impact force. Eddy current sensors record the induced motion while an accelerometer fixed to the load shaft assembly measures its acceleration ($\ddot{z}_{TTB}$). Assuming no axial drag from the aerostatic bearings, the equation of motion (EOM) for the system undergoing axial motions is:

$$M\ \ddot{z}_{TTB} = F_{(t)} - F_{TTB} \tag{7}$$

where $F_{(t)}$ is an applied external load, $F_{(t)} = F_0 + F_{d(t)}$, and F_{TTB} is the TTB reaction force equal to $F_{TTB} = F_{TB0} + F_{TB_d(t)}$.

At equilibrium,
$$F_{TB_{Co}} = F_0 \tag{8}$$

Represent the dynamic component of the TB force as

$$F_{OTB_d(t)} \approx K_{TTB} z_{(t)} + C_{TTB} \dot{z}_{(t)} + M_{TTB} \ddot{z}_{(t)} \tag{9}$$

where K_{TTB}, C_{TTB}, and M_{TTB} are the bearing axial force coefficients (stiffness, damping and added mass, respectively). Hence, Eq. (7) becomes

$$M\ \ddot{z}_{TTB} = F_{d(t)} - K_{TTB} z_{(t)} - C_{TTB} \dot{z}_{(t)} - M_{TTB} \ddot{z}_{(t)} \tag{10}$$

The discrete Fourier transform (DFT) algorithm transforms force, displacement and acceleration data from the time domain into the frequency domain [B3]. Let

$$\bar{z}_{(\omega)} = DFT\left(z_{(t)}\right), \bar{F}_{(\omega)} = DFT\left(F_{(t)}\right), \bar{A}_{(\omega)} = DFT\left(\ddot{z}_{TTB_{(t)}}\right) \tag{11}$$

where ω denotes frequency. Recall that

$$i\omega \bar{z}_{(\omega)} = DFT\left(\dot{z}_{(t)}\right);\ -\omega^2 \bar{z}_{(\omega)} = DFT\left(\ddot{z}_{(t)}\right) \tag{12}$$

where $i = \sqrt{-1}$ is the imaginary unit. Hence, in the frequency domain Eq. (10) becomes

$$H_{(\omega)} = \frac{\bar{F}_{d(\omega)} - M\bar{A}_{(\omega)}}{\bar{z}_{(\omega)}} = K_{TTB} - M_{TTB}\omega^2 + i\omega C_{TTB} \tag{13}$$

Where H is the dynamic (complex) stiffness for the test element. With $H_{(\omega)}$ is obtained, the estimation of the TB axial force coefficients follows from curve fitting of the real and imaginary parts of the complex stiffness, i.e.

$$Re\left(H_{(\omega)}\right) \rightarrow \left(K - M\omega^2\right)_{TTB}, Im\left(H_{(\omega)}\right) \rightarrow C_{TTB}\omega \tag{14}$$

Note M = 3.856 kg based on scale measurements.

Preliminary Experimental Results

Without rotor speed, pressurized water (T=31 °C) supplies the journal bearings at 3.45 bar(g) and lifts the rotor. Water at 3.45 bar(g) supplies the slave and test thrust bearings. The static loader applies a 50 lbf load onto the test thrust bearing, which transfers the load to the rotor thrust collar. The slave thrust bearing, rigidly affixed to the housing, reacts to the applied load. An impact load gun then applies an impact force to the test thrust bearing which reacts to the force. Figure 36 shows the axial impact force applied to the bearing versus time and the DFT amplitude.

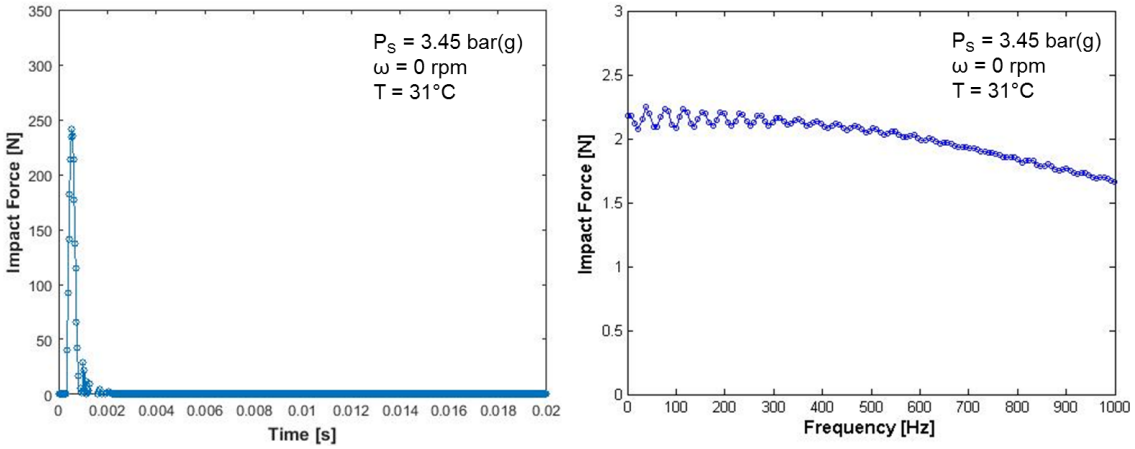

Figure 36. Typical impact force along axial direction and FFT amplitude.

Figure 37 shows the bearing center clearance (C_0) relative to the rotor thrust collar versus time and its DFT amplitude, for a single impact. Note the unusual displacement behavior at low frequencies (less than 200 Hz). Troubleshooting of the load mechanism is

underway in order to better excite the system and conduct a reliable determination of the bearing force coefficients.

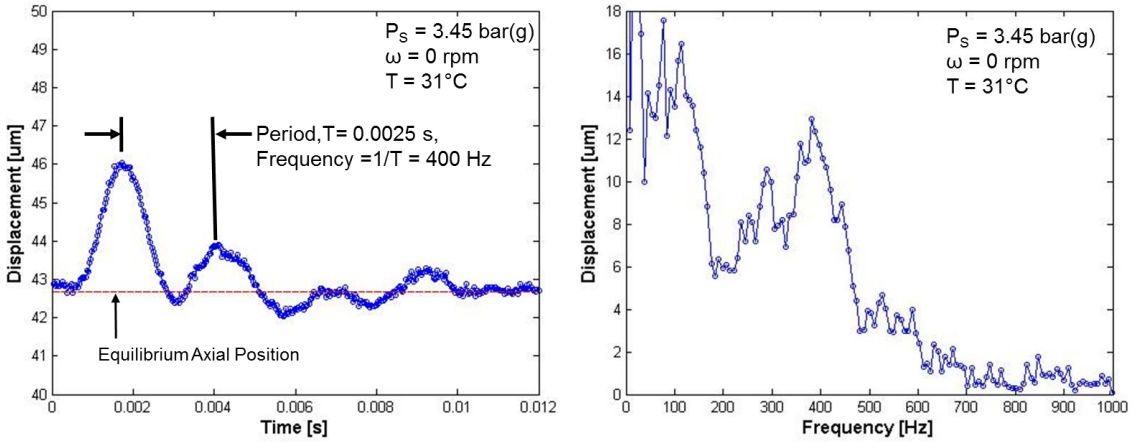

Figure 37. Typical thrust bearing axial displacement with respect to rotor thrust collar versus time and FFT amplitude. Motion due to an impact force along the axial direction. Equilibrium axial position of the thrust bearing is indicated with a straight line.

References

[B1] Tiwari, R., Lees, A. W., and Friswell, M. I., 2004, "Identification of Dynamic Bearing Parameters: A Review," Shock Vib. Dig., **36**, pp. 99–124.

[B2] San Andrés, L., 2014, "Mechanical Vibrations, Numerical solution of EOM for a Single Degree of Freedom (SDOF) system," Notes 6, Texas A&M University Digital Libraries, http://hdl.handle.net/1969.1/93271 [5 April 2016].

[B3] San Andrés, L., 2010, "Modern Lubrication Theory, Experimental Identification of Bearing Force Coefficients," Notes 14, Texas A&M University Digital Libraries, http://hdl.handle.net/1969.1/93254 [5 April 2016].

Appendix C: Predictive Codes for Bearing Performance

XLHydroJet® and XLHydroThrust® predict the force coefficients as well as other performance parameters for hydrostatic journal bearings and hydrostatic thrust bearings, respectively. Tables 7 and 8 show the required inputs and the outputs for XLHydroJet® [13] and XLHydroThrust® [9], respectively. XLHydroJet® links with XLTRC^2® [12], a rotordynamic suite, to produce predictions for a rotordynamic system, such as natural frequency, damping ratio, and imbalance response.

Table 7. Input and output parameters for radial bearings [13].

Inputs	Outputs
Bearing Geometry	Stiffness (Direct and Cross-Coupled)
Pad Geometry	Damping (Direct and Cross-Coupled)
Pocket Geometry	Added Mass (Direct and Cross-Coupled)
Orifice Geometry	Impedances (Direct and Cross-Coupled)
Lubricant Properties	Static Eccentricity
Thermal Options	Mass Flow Rate
Supply Pressure	Static Reaction Force
Exit Pressure	Power Loss
Rotor Speed	Equivalent Stiffness
Excitation Frequency	Whirl Frequency Ratio
Static Load/Static Eccentricity	Drag Torque
Fluid Inertia Presence	Maximum Pressure
Mesh Size	Maximum Temperature

Table 8. Inputs and outputs from XLHydroThrust® [9].

Inputs	Outputs
Bearing Geometry	Force and Moment Stiffness (Direct and Angular Displacements)
Pad Geometry	Force and Moment Damping (Direct and Angular Displacements)
Pocket Geometry	Force and Moment Added Mass (Direct and Angular Displacements)
Orifice Geometry	Clearance
Lubricant Properties	Mass Flow Rate
Thermal Options	Static Reaction Force
Supply Pressure	Power Loss
Exit Pressure	Equivalent Stiffness
Rotor Speed	Whirl Frequency Ratio
Excitation Frequency	Drag Torque
Static Load/Clearance	Maximum Pressure
Fluid Inertia Presence	Maximum Temperature
Mesh Size	

Appendix D: Repeatability of Measurements

During three separate tests, Figures 38-40 show the specific axial load, supply flow rate, and the recess pressure ratio versus axial clearance, respectively, for operation with water (31 °C) at 3.45 bar(g) supplying the radial and thrust bearings as the rotor spins at 3 krpm. Each of these figures demonstrates the repeatability of the tests; thus, evidencing that the results are not dependent on a particular trial.

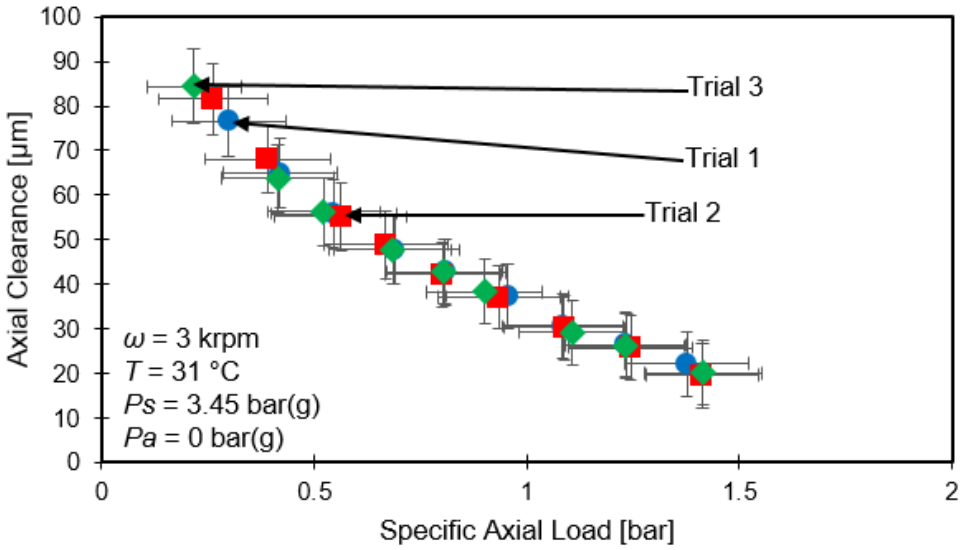

Figure 38. Measured axial clearance of test thrust bearing vs. specific load (*W/A*) for operation with water (31 °C) at a supply pressure (P_S) of 3.45 bar(g) into the thrust bearing. Shaft rotates at 3 krpm. Figure shows three separate trials. Water at 3.45 bar(g) feeds the journal bearings. Ambient pressure (P_a) is 0 bar(g). Vertical and horizontal error bars represent the uncertainty in the axial clearance and the specific axial load at a 95% confidence level, respectively.

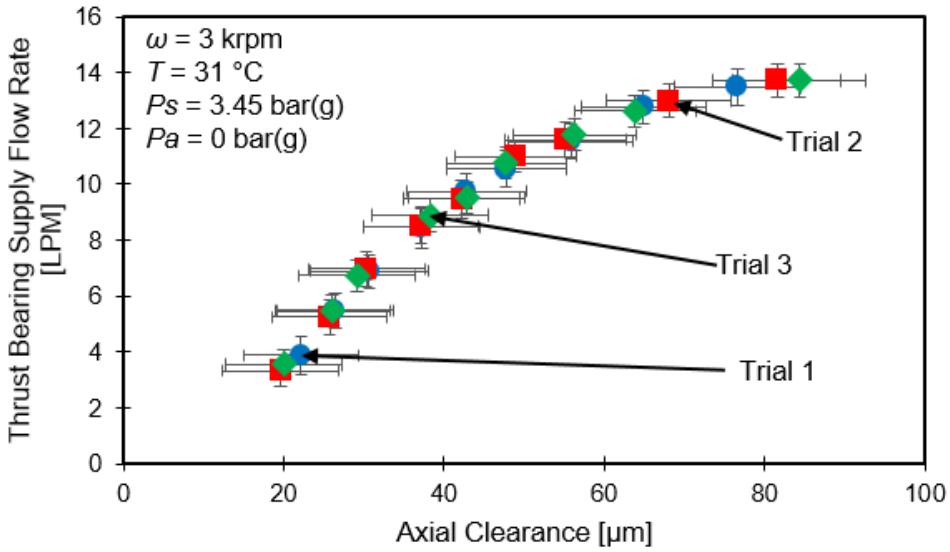

Figure 39. Measured thrust bearing supply flow rate vs. axial clearance for operation with water (31 °C) at a supply pressure (P_S) of 3.45 bar(g) into the thrust bearing. Shaft rotates at 3 krpm. Figure shows three separate trials. Water at 3.45 bar(g) feeds the journal bearings. Ambient pressure (P_a) is 0 bar(g). Vertical and horizontal error bars represent the uncertainty in the thrust bearing supply flow rate and the axial clearance at a 95% confidence level, respectively.

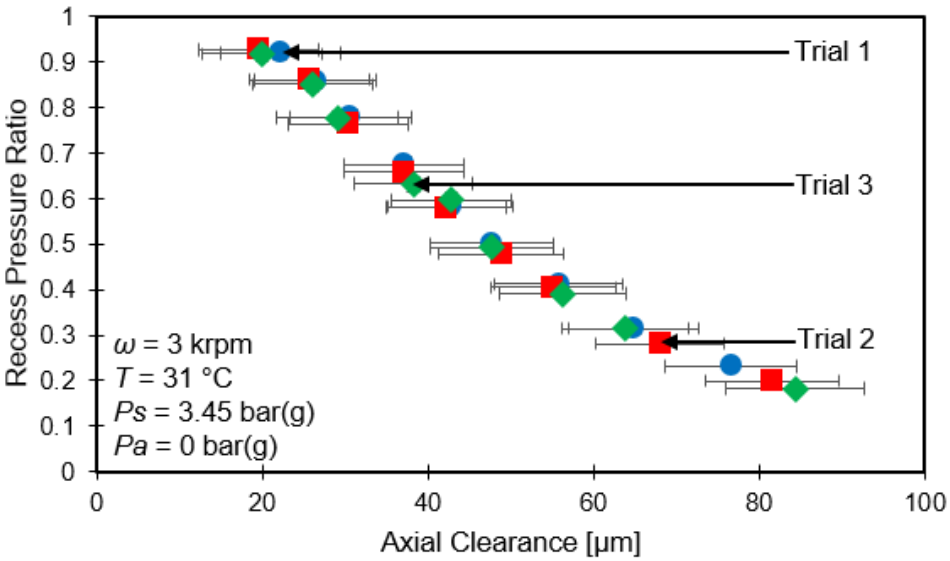

Figure 40. Measured recess pressure ratio vs. axial clearance for operation with water (31 °C) at a supply pressure (P_S) of 3.45 bar(g) into the thrust bearing. Shaft rotates at 3 krpm. Figure shows three separate trials. Water at 3.45 bar(g) feeds the journal bearings. Ambient pressure (P_a) is 0 bar(g). Vertical and horizontal error bars represent the uncertainty in the recess pressure ratio and the axial clearance at a 95% confidence level, respectively.

Appendix E: Thrust Collar Plane Equation Derivation [3]

Eddy current sensors face a thrust collar and measure the axial gap between the thrust collar and TB surface at three circumferential locations, as shown in Figure 41. Using the gap clearances and the geometry to determine the clearance between the thrust collar and the TB surface at the center of the TB and the tilt of the thrust collar relative to the TB is critical in order to estimate the TB performance.

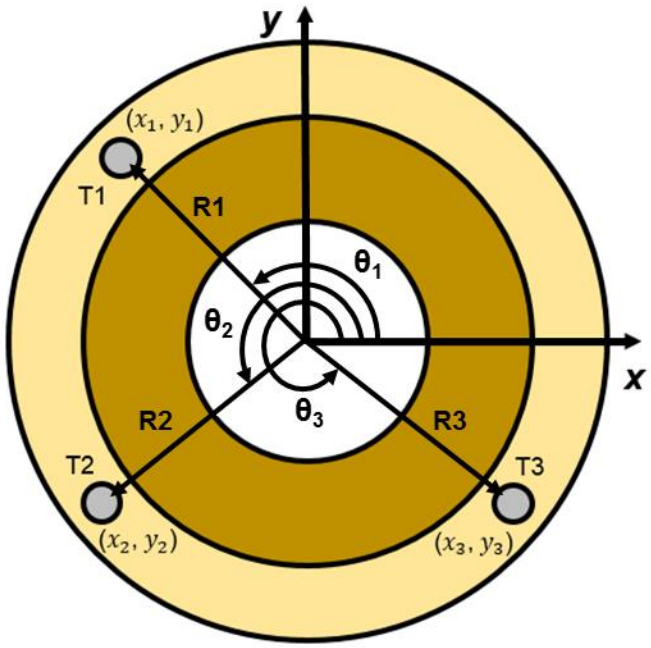

Figure 41. Schematic view of position of eddy current sensors on test thrust bearing.

Table 9 describes the horizontal and vertical position of each eddy current sensor relative to the center of the TB.

Table 9. Horizontal and vertical positions of each eddy current sensor relative to the center of the thrust bearing.

	x	*y*
Probe T1	x_1 = -33.02 mm	y_1 = 27.69 mm
Probe T2	x_2 = -37.34 mm	y_2 = -21.59 mm
Probe T3	x_3 = 37.34 mm	y_3 = -21.59 mm

Assuming the TB and the thrust collar act as rigid planes, the gap between the thrust collar and the TB surface at each eddy current sensor can be used with the position of each eddy current sensor to determine the equation of the plane of the rotor thrust collar relative to the TB. To derive the rotor thrust collar plane equation, first establish a vector to define the distance from the TB center to each sensor and the angle between each vector and the x-axis as,

$$R_i = \sqrt{x_i^{\,2} + y_i^{\,2}} \ , \qquad \theta_i = \tan^{-1}\left(y_i / x_i\right) \ , \tag{15}$$

respectively.

The axial gap at the center of the TB (C_0) as well as the tilt of the rotor thrust collar about the *x*-axis (δ_x) and *y*-axis (δ_y) relative to the TB define the clearance at any point on the thrust collar surface (C_i),

$$C_i = C_0 + R_i \cos\theta_i \delta_y + R_i \sin\theta_i \delta_x \tag{16}$$

which can be simplified to the following form,

$$C_i = C_0 + X_{Si}\delta_y + Y_{Si}\delta_x \tag{17}$$

The transformation matrix,

$$A_T = \begin{bmatrix} 1 & X_{S1} & Y_{S_1} \\ 1 & X_{S2} & Y_{S_2} \\ 1 & X_{S3} & Y_{S_3} \end{bmatrix} \tag{18}$$

enables the conversion of the axial clearance measurements from each sensor (C_1, C_2, and C_3) into C_0, δ_y and δ_x with the following relation,

$$\begin{Bmatrix} C_0 \\ \delta_y \\ \delta_x \end{Bmatrix} = A_T^{\,-1} \begin{Bmatrix} C_1 \\ C_2 \\ C_3 \end{Bmatrix} \tag{19}$$

Appendix F: Uncertainty Analysis of Clearance and Misalignment between Rotor Thrust Collar and Thrust Bearing [15]

The allowable run out in each thrust collar is 5 um. Therefore, there will be an uncertainty of ±5 um when defining the null clearance at each eddy current sensor and an uncertainty of ±5 um when measuring the clearance at each sensor, equating to a total bias uncertainty of ±10 um for each eddy current sensor. The Kline McClintock method, shown below, determine the bias uncertainty in the axial clearance at the center of the thrust bearing (β_{C_0}) and the bias uncertainty in the tilt of the thrust collar about the *x*-axis (β_{δ_x}) and *y*-axis (β_{δ_y}) relative to the thrust bearing based off the bias uncertainty in each sensor ($\beta_{z_1}, \beta_{z_2}, \beta_{z_3}$).

$$\beta_{C_0} = \sqrt{\left(\frac{dC_0}{dz_1}\beta_{z_1}\right)^2 + \left(\frac{dC_0}{dz_2}\beta_{z_2}\right)^2 + \left(\frac{dC_0}{dz_3}\beta_{z_3}\right)^2}$$

$$\beta_{\delta_x} = \sqrt{\left(\frac{d\delta_x}{dz_1}\beta_{z_1}\right)^2 + \left(\frac{d\delta_x}{dz_2}\beta_{z_2}\right)^2 + \left(\frac{d\delta_x}{dz_3}\beta_{z_3}\right)^2} \quad (20)$$

$$\beta_{\delta_y} = \sqrt{\left(\frac{d\delta_y}{dz_1}\beta_{z_1}\right)^2 + \left(\frac{d\delta_y}{dz_2}\beta_{z_2}\right)^2 + \left(\frac{d\delta_y}{dz_3}\beta_{z_3}\right)^2}$$

The standard of deviation and the t-Distribution Table determine the precision uncertainty of each measurement at a 95% confidence level.

$$\xi = t_{\alpha=0.025, df=1000} * \sigma \quad (21)$$

Where

ξ = Precision uncertainty based off 95% confidence level

σ = Standard of deviation

$t_{\alpha=0.025, df=1000}$ = t-table factor for 1000 degrees of freedom at a 95% confidence level

The root sum square of the precision uncertainty and the bias uncertainty defines the total uncertainty of each measurement.

$$\varepsilon = \sqrt{\xi^2 + \beta^2} \tag{22}$$

where

ε = Total uncertainty based off 95% confidence level

ξ = Precision uncertainty based off 95% confidence level

β = Bias uncertainty